

Review

Recent Advances on Transition Metal Chalcogenide for Sodium-Ion Batteries

Chunyan Wei [†], Dongyang Qu [†], Qiuyu Li, Zhonghui Sun [†] , Zhongqian Song, Hongyu Guan ^{*} and Li Niu ^{*} 

College of Chemistry and Chemical Engineering, Guangzhou University, Guangzhou 510006, China; vvcywei@163.com (C.W.); dyqu@gzhu.edu.cn (D.Q.); 19303031354@163.com (Q.L.); cczhsun@gzhu.edu.cn (Z.S.); zqsong@sdfmu.edu.cn (Z.S.)

^{*} Correspondence: guanhy@gzhu.edu.cn (H.G.); lniu@gzhu.edu.cn (L.N.)

[†] These authors contributed equally to this work.

Abstract: Sodium-ion batteries (SIBs) are expected to replace lithium-ion batteries (LIBs) as a new generation of energy storage devices due to their abundant sodium reserves and low cost. Among the anode materials of SIBs, transition metal chalcogenides (TMXs) have attracted much attention because of their large layer spacing, narrow band gap, and high theoretical capacity. However, in practical applications, TMXs face problems, such as structural instability and poor electrical conductivity. In this review, the research progress and challenges of TMXs in SIBs in recent years are summarized, the application of nanostructure design, defect engineering, cladding engineering, and heterogeneous construction techniques and strategies in improving the electrochemical performance of TMXs anode are emphatically introduced, and the storage mechanism of sodium is briefly summarized. Finally, the application and development prospects of TMX anodes in electrochemical energy storage are discussed and prospected.

Keywords: sodium-ion batteries; transition metal chalcogenide; challenges



Citation: Wei, C.; Qu, D.; Li, Q.; Sun, Z.; Song, Z.; Guan, H.; Niu, L. Recent Advances on Transition Metal Chalcogenide for Sodium-Ion Batteries. *Batteries* **2023**, *9*, 467. <https://doi.org/10.3390/batteries9090467>

Academic Editor: Catia Arbizzani

Received: 23 August 2023

Revised: 8 September 2023

Accepted: 13 September 2023

Published: 16 September 2023



Copyright: © 2023 by the authors. Licensee MDPI, Basel, Switzerland. This article is an open access article distributed under the terms and conditions of the Creative Commons Attribution (CC BY) license (<https://creativecommons.org/licenses/by/4.0/>).

1. Introduction

Since LiCoO_2 was first commercialized as the LIB anode electrode, the development of LIBs has matured and been widely used in various electronic products, energy storage systems, and other fields in just thirty years due to their high energy density and excellent cycling performance [1]. According to USGS statistics, by 2020, the global lithium reserves are about 21 million tons of metal, but the annual lithium consumption is more than 85,000 tons and continues to rise every year. The low reserves and high consumption of lithium crust, as well as the resulting resource shortage and cost problems, make it difficult to sustain the large-scale application of LIBs [2,3]. The current development of LIB technology is relatively mature, but due to the use of flammable organic electrolytes and the strong activity of lithium metal, it is still prone to fire, thermal runaway, and other safety hazards [4]. In this case, various types of energy storage devices have been developed to meet the needs of development. The development is currently limited due to various reasons, such as the Li-Se battery's electronic transfer ability being excellent and the theoretical volume capacity being high, but the volume expansion is serious and the utilization rate of active substances is not high, so the capacity attenuation is serious. Water-based zinc-ion batteries have a low cost, small size, light weight, and good safety, but zinc dendrite growth is serious, and energy density is limited. Supercapacitors have excellent power density, long lifecycles, and a friendly raw material environment, but the production cost is high, and the energy density is low [5–8]. Sodium is a neighboring element in the same group as lithium, and the two have similar physical and chemical properties, closer electrode potentials (only 0.3 V difference with lithium), and analogous ion storage mechanisms. In addition, the sodium reserves in the Earth's crust are far more abundant than lithium resources, and easy extraction can effectively reduce production costs; they

are expected to replace LIBs as the main force of future energy storage utilization [9–12]. However, because the radius of Na-ion is much larger than Li-ion, the layer spacing of the host material is required to meet the Na⁺ insertion/extraction, resulting in a large number of anodes that can work for SIBs [13]. Therefore, the development of host materials with large interlayer spacing and excellent electrochemical properties is the key to the large-scale application of SIBs.

Various kinds of electrode materials have been investigated in the development of SIBs. The charge storage mechanism in SIBs can be divided into insertion-type materials (such as graphite and other carbonaceous materials, TiO₂, etc.), alloying-type materials (such as Bi, As, Si), and conversion-type materials (such as various transition metal compounds). Insertion-type anodes have low volume change but low specific capacity, alloying-type materials have high capacity but significant volume change (volume expansion even higher than 400%), and conversion-type materials are just in between and have received a lot of attention [11,14,15]. As a representative of the transition metal chalcogenide with large layer spacing, a narrow band gap (exhibiting metal-like behavior and high conductivity when narrow enough) and a high theoretical capacity (transferring multiple electrons per metal center; the capacity of selenide can reach 500–1000 mAh g⁻¹), they are currently the hot spot in the research of negative electrode materials [16–23]. Transition metal chalcogenides (TMXs) are located in the VIA group of the periodic table, containing the elements O, S, Se, Te, and Po. Due to the large difference in physical and chemical properties between oxygen and other chalcogen elements and the low abundance of Te in the crust, only transition metal sulfides and transition metal selenides are considered in this review. TMXs have the structure of lamellar (M generally IVB–VIIB group transition metals) and non-lamellar (M generally VIII–X group), in which the lamellar structure consists of X-M-X connected in the form of covalent bonds to form a lamellar plane, and the layers are coupled by weak van der Waals forces, often creating a single or multilayer lamellar structure. The interlayer spacing of TMXs with lamellar structures is usually 6–7 Å (much more prominent than 1.02 Å for sodium ions), which can tolerate Na⁺ to break through the weak van der Waals forces between the layers for conversion reactions [24,25]. However, serious volume expansion, slow Na⁺ diffusion kinetics, and insufficient electrical conductivity often occur in practical applications, resulting in poor SIB cycling stability, short battery life, and lower rate capability.

In this review, we present the research status of TMXs in SIB-negative electrodes, briefly introduce the sodium storage mechanism of TMXs, and highlight the fundamental problems and corresponding optimization strategies in their practical application, as shown in Figure 1.

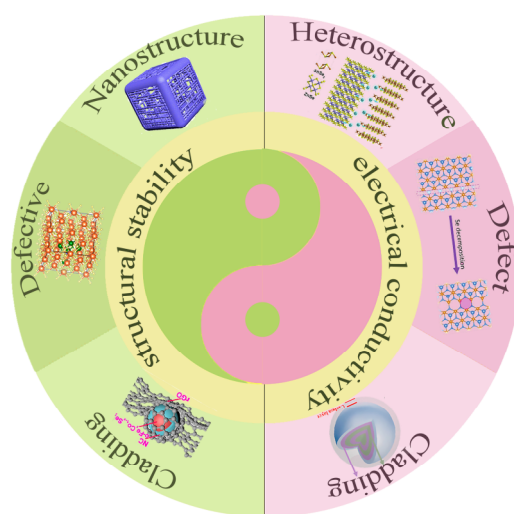
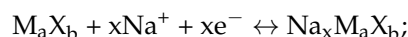


Figure 1. Challenges and strategies for TMXs as the anode in SIBs.

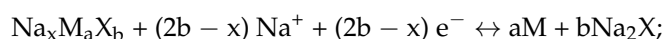
2. Sodium Storage Mechanism

Studying the sodium storage mechanism of batteries is an essential basis for the rational design of electrode materials and for improving their battery performance. TMXs will generally undergo intercalation, conversion, or alloying reactions and electrochemical reactions of the pseudocapacitor energy storage mechanism in a specific voltage range. In non-layered materials, the sodium ion embedding pathways are diverse, and the sodium storage mechanism is more complex and will not be outlined in this review. For layered materials, Na^+ tends to embed between atomic layers, and different electrochemical reactions occur with the change in voltage range. In the high voltage range, the intercalation reaction of sodium ions mainly occurs, and then the decrease in voltage, conversion reactions occur to produce metal monomers (M) and the corresponding chalcogenide sodium compounds (Na_nX) [26]. If the obtained metal monomer M has particular activity, it can also continue to undergo alloying reactions with sodium ions. Based on the above discussion, the whole process can be described as follows [27]:

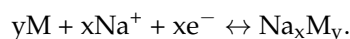
1. Intercalation process of the sodium ions:



2. Transformation reactions (generally transition metal-based chalcogenides, such as Co, Ni, Cu, etc.) occur:



3. Alloying reactions (often occurring in Bi, Sn-based, and other sulfuric materials with some metal activity):



It was found that the LIB storage mechanism of the layered material MoS_2 is a typical reaction of intercalation before conversion, and the reaction products are mainly metal Mo and LiS_2 . The SIB storage mechanism is similar to LIBs and should follow the same mechanism [28]. However, this is not the case, according to Wang's research group [29]. Through electronic PDF analysis (Figure 2a) of $\text{MoS}_2\text{-C@C}$ composite material, Wang's research group found that the Mo-S bond peak still dominates after naturalization, which means that MoS_2 does not break the Mo-S bond to obtain the metal Mo and its sodiation products after the conversion reaction. Instead, distorted MoS_x polyhedral clusters were obtained as new active substances for sodium storage, and the absence of Mo in the metallic phase was further verified by XAS spectra (Figure 2b,c). Figure 2d is a summary of the sodium storage mechanism. To exclude the interference of carbon, Wang's research group also investigated the sodium storage process of carbon-free MoS_2 and showed that although the structural evolution of carbon-free MoS_2 is like $\text{MoS}_2\text{-C@C}$ composites in that MoS_x clusters are obtained, this process is irreversible, which leads to its worse cycling performance that revealed the stabilizing effect of carbon on MoS_x clusters (as shown in Figure 2e,f) [29].

Previous studies proposed that the sodiation process of MoSe_2 should undergo an intercalation reaction and alloying reaction [30]. When Yang's research group [27] investigated the sodium storage mechanism of $\text{SnSe}_2\text{-3D}$ through non-in situ XRD, they found that the alloying reaction between the active metal and sodium may also occur during the actual sodalization/desodalization process and that multiple alloying products may coexist (Figure 2g,h). With the continuous insertion of Na^+ , the two peaks (14.4, 44.1) of SnSe_2 at 1.6 V gradually diminished (the intercalation product Na_xSnSe_2 was obtained) and completely disappeared at 0.9 V (the conversion products Na_2Se and Sn were received, and the active metal Sn continued to alloy with Na^+). At this time, a peak of the NaSn_n alloy appeared, indicating that the alloying reaction occurred at a voltage of 0.9 V. While continuously discharging reaches 0.7 V, another $\text{Na}_{29.58}\text{Sn}_8$ alloy peak appeared; when it was ultimately discharged to 0.01 V, the peak of the $\text{Na}_{15}\text{Sn}_4$ alloy with higher sodium content occurred. At this time, the peak of the intermediate $\text{Na}_{29.58}\text{Sn}_8$ alloy disappeared,

and the heights of the $\text{Na}_{15}\text{Sn}_4$ and NaSn alloys coexisted. As charging continued to 1 V, the peak of the intermediate $\text{Na}_{29.58}\text{Sn}_8$ alloy reappeared, demonstrating the highly reversible reaction of the alloy, and it was not until charging reached 2.9 V that the alloy product was consumed entirely [27]. To gain more profound insights into the sodium storage mechanism of MoSe_2 , Plewa's research group [31] combined operando XRD and in situ XANES and XPS analyses to propose that the sodiation of MoSe_2 undergoes three processes in sequence: alloying, intercalation, and conversion reactions. In the initial cycle, the formation of Se precipitation was observed at 0.8 V (which was not reported before), and the active Se was alloyed with Na^+ to produce Na_2Se until the end of the intercalation reaction at 0.5 V, during which the intercalation product Na_xMoSe_2 underwent a transformation reaction to obtain the metallic Mo and Na_2Se phases. Plewa's research also found that after the first cycle, MoSe_2 was converted from the pristine hexagonal 2H phase to the 1T phase with enhanced transport properties, and in further cycles, 1T- NaMoSe_2 was used as the starting point for the intercalation reaction [31].

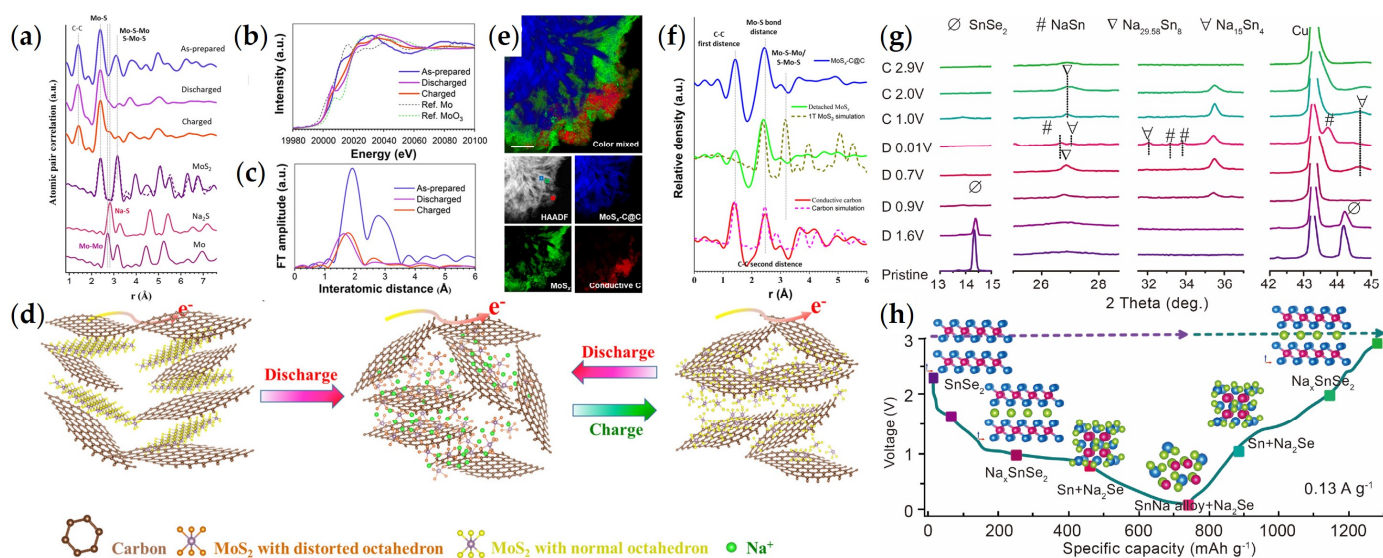


Figure 2. (a) PDF analysis of the crystal structure; (b) XAS spectrum; (c) FT-EXAFS; (d) STEM-PDF map after the first cycle; (e) PDF curves; (f) schematics of the proposed desodiation/sodiation mechanism; (g) ex situ XRD and (h) sodium storage mechanism of $\text{SnSe}_2@3\text{D}$ [27,29].

In addition, the electrochemical reaction of the pseudocapacitive energy storage mechanism also exists in TMXs. Pseudocapacitors include intrinsic pseudocapacitors and non-intrinsic pseudocapacitors. Intrinsic pseudocapacitance means that the material exhibits pseudocapacitive behavior in all morphologies or particle sizes, while non-intrinsic pseudocapacitance generally occurs exclusively at and near the surface of nanomaterials. The pseudocapacitance behavior can suppress the phase transition process and increase Na^+ adsorption capacity and the rapid Na^+ diffusion kinetics. Yuan's research group [32] prepared atomically thin $\text{Co}_{1-x}\text{Se}_2/\text{graphene}$ heterostructures and proved that the Co vacancy in the heterostructure is essential in improving the electrochemical performance. According to the CV curves at different scan rates, the low scan rate ($50\text{--}100\text{ mV s}^{-1}$) is diffusion-controlled (embedding/transformation/alloylation process). The high scan rate is a capacitation-dominated electrochemical process (pseudocapacitance process). The presence of Co vacancies enhances this pseudocapacitance behavior and further reveals that the improved electrochemical performance contributes to the enhancement of the pseudocapacitance of the intercalation layer [32]. Lin's research group [33] fabricated N-doped C-coated Ni-Co bimetallic sulfide hollow nanocube ($(\text{Ni}_{0.5}\text{Co}_{0.5})_9\text{S}_8 @\text{NC}$) composites and investigated their sodium storage mechanism, with a predominant pseudocapacitance storage behavior (the pseudocapacitance contribution reaches 90% at high scan rates). Next, the Operando XRD analysis found that Na_2S , Ni, Co, and Na_2S_5 were obtained successively

with the progress of sodiation, which was also the first time that Na_2S_5 was observed in TMXs. Its formation may be attributable to the more abundant chemical composition of the bimetallic sulfide [33].

3. Optimization Strategy for Increasing Sodium Reserves

3.1. Enhanced Structural Stability

In the practical application of the battery, with the conversion of electrode materials and alloying reaction, the initial lattice structure of the material will be destroyed and will inevitably produce massive volume expansion. On the one hand, the stress generated in the volume expansion process continues to accumulate, which eventually causes the electrode particles to crack or even crush, and some active materials lose their electrochemical activity. On the other hand, for the entire electrode, the volume expansion will lead to the collapse of the electrode material structure, which will cause the electrode material to fall off the electrode surface, resulting in capacity decay [34]. Therefore, researchers have conducted much research and proposed many effective solutions, including the design of nanostructure engineering, defect engineering, and coating engineering for electrode materials.

3.1.1. Nanostructure Engineering

Various relevant reports have proved that by adjusting the size and dimension of the material, the electrode material can be endowed with excellent electrochemical performance. The transformation from bulk to nanomorphology must only reduce the size to less than 100 nm. So far, various structures and forms of nanostructures have been widely reported, such as quasi-zero-dimensional quantum dots, zero-dimensional nanoparticles (NPs), one-dimensional nanotubes/wires/rods, two-dimensional nanosheets, and three-dimensional network structures [35–37]. The structures of the nanomaterials in each dimension and their advantages and disadvantages are summarized, as shown in Figure 3 [38]. Compared with bulk materials, nanostructured materials have higher specific surface area and higher average binding energy of surface atoms, so they can better release stress in the process of volume expansion and avoid the collapse of their structures. It is worth noting that nanomaterials can reduce the volume expansion in the repeated cycle process by reducing the dimension. For example, Guo's research group [39] formed ultra-small CoS_x quantum dots (average particle size 3~5 nm) in situ on ultra-thin (about 4.5 nm) n/s co-doped folded 2D carbon nanosheets, showing outstanding electrochemical performance. The ultra-small size of the quantum dots has slight strain and can withstand significant volume changes without breaking, and the particle diffusion path is shortened, which dramatically improves the electrochemical reactivity of the material [34,38,40].

Although the reduction in particle size shortens the Na^+ diffusion path and makes the particle/electron transfer process more accessible, it can also withstand the influence of stress in volume expansion. Due to the reduction in particle size, the parasitic reaction between small particles and the electrolyte interface will also increase, which may lead to the repeated formation and decomposition of the solid electrolyte interface layer and consume more electrolytes. On the other hand, the smaller the nanoparticles (especially 5~10 nm), the more serious the agglomeration and inactive clusters [41,42]. One solution to these potential defects is introducing carbon materials as a buffer matrix. Carbon materials can protect active materials from direct contact with electrolytes, enhance the conductivity of electrode materials, and reduce volume changes [43–45]. Chen's research group [46] proposed that the ultra-small Co_9S_8 quantum dots were embedded in mesopore hollow carbon polyhedra, and the outer layer was coated with gridded redox graphene. The double carbon layer could prevent nanoparticle aggregation and excessive growth, thus showing excellent cyclic stability [46]. Another approach is adding growth inhibitors to the pyrolysis process to prevent nuclei growth and obtain sub-nanometer particles [47,48]. Cheng's research group [49] used electrospinning technology to obtain N/S-containing polymer fibers and performed pre-oxidation and vulcanization treatment. In the pre-

oxidation process, LiN_3 was used as a growth inhibitor to prevent Sn-O intermediates from aggregating and crystal nucleus growth during the subsequent vulcanization process, and SnS quantum dots (SnS QDs@NCF) with smooth surfaces of N-doped carbon fibers were finally obtained. In contrast, SnS nanoparticles were produced on the surface of polymer fibers and received SnS nanoparticles (SnS@NCF) without the LiN_3 inhibitor. In subsequent electrochemical tests, the advantage of the quantum dots and the protection of the carbon matrix enabled the SnS QDs@NCF to exhibit superior cycling performance (430.9 mAh g^{-1} after 7880 cycles at 10 A g^{-1}), while SnS nanoparticles grown directly on the carbon fiber surface were susceptible to shattering and detachment from the fiber surface, resulting in a rapid decrease in capacity [49].

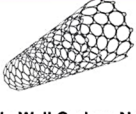
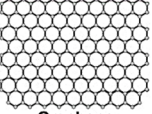
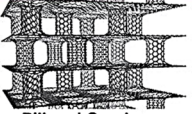
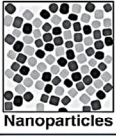
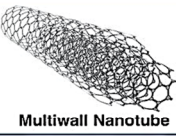
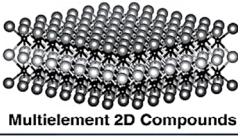
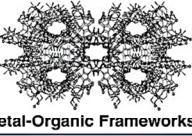
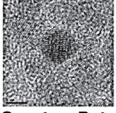
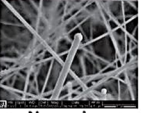
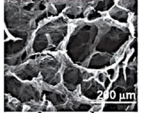
0D	1D	2D	3D
 Carbon Onion	 Single Wall Carbon Nanotube	 Graphene	 Pillared Graphene
 Nanoparticles	 Multiwall Nanotube	 Multielement 2D Compounds	 Metal-Organic Frameworks
 Quantum Dots	 Nanowires	 Nanoflakes	 Aerogels
Advantages			
Small in all dimensions Surfaces on all sites are accessible to electrolytes No bulk solid-state diffusion Can be integrated into multiple systems Can be used in stable inks for printing	Mechanical reliability Possibility to integrate with wearable devices Porous flexible freestanding films	Open 2D channels for ion transport; all surface is accessible enabling fast charge storage Compatible with flexible devices Small nanoflakes can be used in inks for printing	Can be used to create thick electrodes with large areal and volumetric storage properties
Limitations			
Agglomeration Do not densely and form only low density non-uniform structures Numerous points of contact lead to high resistance Poor chemical stability	Low packing density; cannot exhibit high volumetric performance Low yield and high cost of synthesis Diffusion pathways can be relatively long	Re-stacking Low out-of-plane electronic and ionic conductivity High cost of synthesis	Design Stability Manufacturing

Figure 3. Overview of the 0D, 1D, 2D, and 3D nanomaterials [38].

One-dimensional (1D) nanomaterials (nanotube/wire/rod/fiber) have a short diameter and a long ion diffusion path. The short diameter can reduce the occurrence of volume expansion, the electron/particle transfer in the longitudinal direction can increase the conductivity of the material, and the smaller radial size can significantly improve the diffusion kinetics of sodium ions [50,51]. Xu's research group [52] prepared yolk-shell-like ZnS@C nanorod electrodes with a porous structure using $\text{Zn}_2\text{GeO}_4\text{@C}$ as a self-sacrificing template, and the unique design maintains good capacity. The main reason is that the porous structure possessed by this yolk-shell nanorod introduces a large number of voids, which alleviates the volume stress caused by sodium ions in repeated cycles. One-dimensional nanowires are also attractive. In addition to being able to adapt to volume strain, their larger aspect ratio than nanorods expose more active surfaces for charge transfer between the electrolyte and the nanorod and provide a stable unidirectional electron transport path to improve the conductivity and dynamics of the electrode [52]. Yang's research group [53] used Se/C nanowires as a template to obtain carbon-loaded nickel selenide ($\text{Ni}_{0.85}\text{Se/C}$)

hollow nanowires by continuously dissolving the inner selenium and forming $\text{Ni}_{0.85}\text{Se}$ nanoparticles on the surface of the carbon layer during the reaction with Ni^{2+} , which eventually exhibited excellent cycling stability (after 2000 cycles at 1 A g^{-1} , the capacity retention was 89%). In addition to preparing hollow nanowires, the strong coupling of nanowires with carbon can also enhance structural stability. Wei's research group adopted a simple one-step chemical vapor deposition (CVD) strategy using thiourea formaldehyde resin as a precursor to react with metal foam. In this process, part of the solid thiourea formaldehyde resin formed TMX nanowires with the metal foam, while the other part was transformed into a nitrogen and sulfur co-doped ultra-thin carbon layer, which was tightly and evenly coated on the surface of the nanowires, and the TMXs@NSC nanowire was finally obtained (T for Fe, Co, and Cu). The strong bond cooperation between the carbon layer and TMX nanowires also constructs a heterostructure, enhancing the conductivity with heteroatom defects [54]. Hong's research group [55] prepared $(\text{Co}_{1/3}\text{Fe}_{2/3})\text{Se}_2$ nanofibers with a tube-in-tube fiber structure by electrostatic spinning, and the layered structure of the tube-in-tube resulted in a lower charge transfer resistance and more minor volume expansion, exhibiting superior rate performance compared to conventional TMXs.

Two-dimensional (2D) nanomaterials (nanosheets) generally have layered structures, such as VS_2 [56] and MoS_2 [57], within which electrons can move at very high velocities and usually have high theoretical capacities. However, in practical applications, the large radius of Na^+ causes severe volume expansion when it travels through the 2D nanomaterials, resulting in reduced cell cycle stability. To solve this problem, some researchers have proposed to combine 2D nanomaterials with high-cycle stability skeletons to construct three-dimensional (3D) cross-linked structures. For example, Yuan's research group [58] combined MoS_2 with a 3D Nb_2CT_x MXene framework to form a 3D cross-linked hybridized morphology and finally coated the surface with polydopamine to further enhance the stability of the 3D framework. When used as the anode of SIBs, it has only 0.01% degradation per cycle in 2000 cycles at 1.0 A g^{-1} . The stability performance is excellent because on the one hand, the 3D Nb_2CT_x MXene framework provides a channel for sodium ion diffusion to alleviate the volume change during sodium ion intercalation. On the other hand, the carbon coating coated on the surface has a certain volume elasticity and ensures the stability of the 3D framework [58]. In addition, the formation of pores on the surface of the 2D material is also a good choice. On the one hand, porosity can increase the active surface sites, shorten the Na^+ diffusion distance, and accelerate the charge transfer kinetics; on the other hand, the high mechanical strength of the 2D material can maintain the stability of the porous structure [59,60].

Three-dimensional nanomaterials normally have a large surface area, abundant active sites, ample internal space, and possess higher electrode density and structural integrity than zero-, one-, and two-dimensional materials. Li's research group [61] used a self-templating method to evenly wrap ZnSe nanoparticles in a 3D porous N-doped carbon matrix to obtain popcorn sphere-like composites, and due to the existence of gaps in the porous 3D structure of the nanoparticles to alleviate the volume change stress, they ultimately exhibited favorable cycle stability. However, the synthesis of 3D nanomaterials by the template method has high energy consumption and preparation costs, and the process is also tedious. In recent years, the template-free way has been very attractive for synthesizing 3D nanomaterials. Ge's research group [62] constructed 3D N-doped carbon-layered hollow spheres with double carbon layers using a template-free self-assembly process, in which ultra-thin WS_2 nanosheets were uniformly embedded to obtain an expanded layer spacing and exhibited high structural stability. Park's research group [63] synthesized 3D structured microspheres with multiple chambers and uniform distribution of carbon nanotubes by spray pyrolysis, and the multi-component metal selenide $(\text{NiFe})\text{Se}_x$ graphitic carbon/carbon nanotube composites $(\text{NiFe})\text{Se}_x/\text{GC}/\text{CNT}$ could be obtained by subsequent selenization treatment, as shown in Figure 4a. The uniform distribution of nanopores on the surface and the unique multi-chamber structure improve the material's electrical conductivity and structural stability [63].

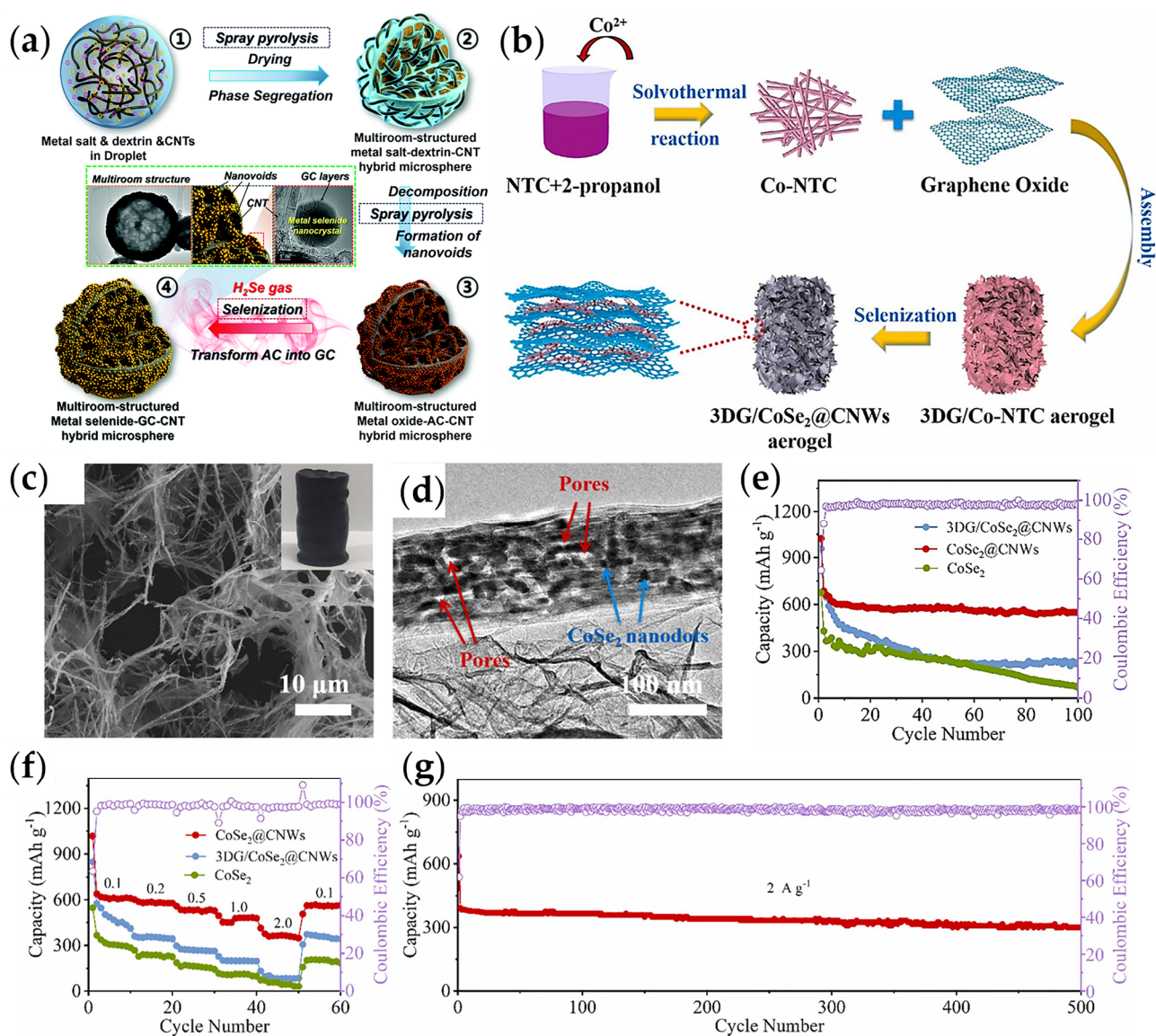


Figure 4. (a) A schematic diagram of the preparation process of multicompartamental structured (NiFe)Se_x/GC/CNT hybrid microspheres; (b) a schematic diagram of the preparation process of multidimensional 3DG/CoSe₂@CNWs; (c) SEM; (d) TEM; (e–g) electrochemical performance of the 3DG/CoSe₂@CNWs anode [63,64].

In addition, constructing multidimensional composites is also an excellent option for taking advantage of the nanomaterials in each dimension of the same material. For example, Xiao's research group [64] synthesized porous multidimensional nanocomposites 3DG/CoSe₂@CNWs by confining 0D CoSe₂ nanodots in 1D carbon nanowires and finally encapsulating them in 3D graphene (Figure 4b). SEM and TEM images can be observed (Figure 4c,d), in which the advantages of each dimensional nanostructure can be fully exploited, exhibiting excellent sodium storage performance (Figure 4e–g). In addition, various structural designs, such as porous, hollow, and yolk-shell structures, have been proposed to resolve the volume expansion question in recent years. Although good progress has been made, such materials are often unable to combine excellent cycling properties with high rate capabilities. To address this problem, Shang's research group [65] sculpted the hollow Cu_{1.75}S cubic precursor into a truss structure using the "selective reduction" strategy using Fe³⁺ and then strengthened it by recrystallization process to obtain Cu_{1.81}S with a truss structure, which is exceptionally stable due to its unique triangular support. The

highly durable truss structure gives excellent cycling stability and high rate performance (331 mAh g^{-1} at 3 Ag^{-1}) when used as an SIB anode electrode.

The biggest difference between 0D, 1D, 2D, and 3D materials is mainly the difference in nanometer size. Zero-dimensional materials have three dimensions in nanometer size, which can provide more active sites for ion adsorption and alleviate volume changes. However, the agglomeration caused by small size is very serious, and it needs to be combined with other materials to alleviate this problem [41,42,66]. One-dimensional materials have two dimensions in nanometer size and a high aspect ratio, which are conducive to rapid electron transmission. However, such materials often have low packing density, high preparation cost, and low yield, and are difficult to be applied on a large scale [50,51,67]. Two-dimensional materials have the advantages of large surface area and adjustable interlayer spacing, but low ion mobility and complex preparation technology limit their development. Compounding with other materials or doping heteroatoms may be the key to solving this problem [68,69]. Three-dimensional materials mean that electrons can move freely on three non-nanoscale scales, which can obviously solve the aggregation problem faced by 0D, 1D, and 2D materials, and the large internal space can alleviate the impact of volume expansion. At the same time, they have an incomparable mechanical stability compared with other dimensional materials but will result in a low initial coulomb efficiency. They can be combined with other dimensional materials to solve this problem [70–72]. To sum up, if further innovative development of 3D materials can be carried out, it may bring new enlightenment to the future development of TMX-negative electrode materials.

3.1.2. Defect Engineering

Since the electrochemical performance of electrode materials is closely associated with the internal crystal structure and composition of the materials, the introduction of defects inside the materials through defect engineering cannot only provide more reactive sites and increased surface energy but also be beneficial to keep the structural stability of the materials, thus regulating the electrochemical performance [73,74]. Crystal defects can be divided into intrinsic defects and extrinsic defects. Inherent defects are caused by the irregular arrangement of local atoms in the crystal itself and will not affect the composition of the whole crystal, such as non-integral compounds. Huang's research group [75] prepared ultra-thin layered porous non-integrable $\text{Co}_{0.85}\text{Se}$ nanosheets, which were also grown vertically on graphene to achieve a 3D porous structure to improve electrical conductivity. XPS results show that Co^{2+} and Co^{3+} present in the crystal form Co vacancy defects as a result of uneven charge distribution, and the presence of vacancies enhances sodium storage kinetics and demonstrates high reversible capacity (at 0.5 A g^{-1} , the reversible capacity has 460 mA h g^{-1}) when used as an SIB anode [75].

In contrast, non-intrinsic defects are introduced by foreign heteroatoms, such as heteroatom doping. Heteroatom doping often causes lattice defects, which can affect the electronic structure and chemical properties of materials by regulating the surface reaction kinetics and long-range disorder, which are vital in stimulating the charge transfer process and increasing the reactive site [76,77]. Zhang's research group [78] prepared $\text{Fe}_7\text{Se}_8/\text{N}$ -CNF composites with open structures by anchoring ultra-small Fe_7Se_8 nanoparticles in N-doped carbon nanofibers. Raman spectroscopy and XPS reveal many defects in the N-doped $\text{Fe}_7\text{Se}_8/\text{N}$ -CNF composite, which exhibits excellent electrochemical reaction kinetics. In recent years, the introduction of O or S vacancies in metal chalcogenides to improve the sodium storage properties of SIBs has attracted much attention. Li's research group [79] introduced ZIF-8 to the surface of WS_2 nanorods by delicate design, and the interaction of ZIF-8 with WS_2 nanorods after calcination resulted in S vacancies and WS_2/ZnS heterojunctions and the formation of a coaxial carbon coating with WS_2 nanorods, which has a unique structure to maintain a favorable reversible capacity after 5000 cycles at a high rate. After the introduction of vacancies, excess electrons will be generated around specific metal atoms and become negative centers, which can attract the

surrounding positive ions and accelerate the transfer of ions, in addition to providing more active sites for sodium storage [79].

3.1.3. Cladding Engineering

The carbon coating evenly coated on the surface of TMXs can not only increase the conductivity of the material but also form a protective layer to separate the electrode material from the electrolyte and protect the internal structure of the electrode from damage. Generally speaking, the carbon coating includes two types: core-shell structure and yolk-shell structure. Lin's research group [33] produced N-doped carbon-coated $(\text{Ni}_{0.5}\text{Co}_{0.5})_9\text{S}_8$ composites using phenol formaldehyde as the carbon cladding, and the synergistic action of each part of the structure resulted in excellent capacity retention at high current densities. Despite the construction of the core-shell structures can enhance the structural stability of the material, the close contact between the coating and the material in the core-shell design can cause the coating to rupture during the cycle, resulting in the collapse of the material structure and ultimately the deterioration of the cycle performance, the cycling performance decreases. To solve this problem, the researchers proposed a double carbon layer structure with more robust mechanical properties. The unique double carbon layer structure can provide more active sites for Na^+ storage due to the increased carbon layer, and the double carbon layer protection can also better alleviate the stress accumulation during repeated cycling. Su's research group [80] prepared MoSe_2 nanorod composites ($\text{MoSe}_2@\text{NC}@r\text{GO}$) with N-doped carbon matrix and graphene double carbon protection by the self-sacrificial template method, As shown in Figure 5a, SAED pattern images (Figure 5b) show that the formation of the double carbon layer is when a layer of carbon is first coated on the surface of the nanorod MoSe_2 , and then graphene is coated on the outermost layer. The experimental results and theoretical calculations show that the existence of the double carbon layer with high conductivity not only gives the composite structure a high Na^+ diffusion coefficient and enhances the reaction kinetics but also can form a solid shell to accommodate the volume change in MoSe_2 -active material and the shuttle of polyselenide, which eventually shows excellent electrochemical performance. When assembled with $\text{Na}_3\text{V}_2(\text{PO}_4)_2/\text{C}$ as a full cell, the cycling performance is promising, as shown in Figure 5c–h [80].

Unlike the ultra-thin, compact core-shell structure formed only by direct coating on the material surface, the yolk-shell structure can introduce a gap between the coating and the material surface. The formation of void space enables the yolk-shell structure to expand/contract more freely than the core-shell structure and can accommodate the volume expansion of internal active substances based on maintaining the stability of the shell, thus improving the strength of the overall structure [81]. Polydopamine can be used to coat almost most materials, and its ability to dope its N atoms into the carbon matrix while forming a protective coating makes it very attractive for material coating [82]. Xu's research group [52] used polydopamine-coated Zn_2GeO_4 precursor nanorods as self-sacrificing templates, and the Ge source dissolved during the vulcanization process, which eventually transformed the core-shell structure nanorod precursor into a porous yolk-shell $\text{ZnS}@C$. Liu's research group [83] used a polydopamine-coated yolk-shell $\text{SnSe}_2/\text{ZnSe}$ nanobox. When used as an SIB anode, the reversible capacity remained at 616 mA h g^{-1} after 1000 cycles at 1 A g^{-1} . An important reason for the excellent reversible capacity was the elastic polydopamine coating, which promoted the charge transfer process, enhanced the conductivity of the material, and prevented the volume change and stress accumulation of the material during repeated cycles, improving structural stability [83]. Polypyrrole has good electrical conductivity due to its conjugated structure, and the nitrogen atom in polypyrrole can chemically bind to polysulfides to restrain the "shuttle effect" of polysulfides, which can also mitigate the volume change during cycling due to its good flexibility and self-healing ability when used as a cladding material [84]. Zhang's research group [85] prepared yolk-shell FeS_2 nanocages using polypyrrole-coated Prussian blue precursors, which retained 92% capacity at 5 A g^{-1} for 1000 cycles.

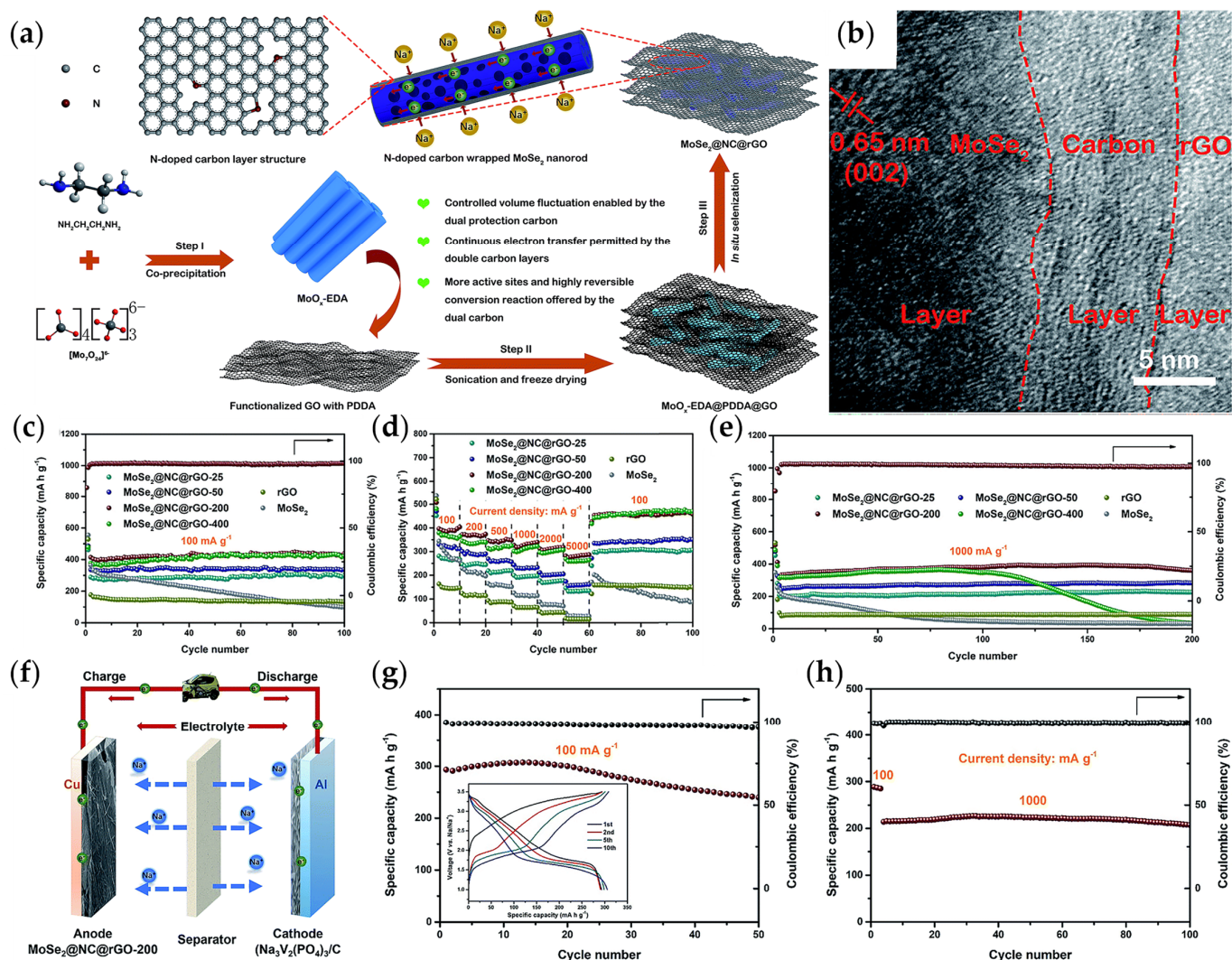


Figure 5. (a) A schematic diagram of the synthetic process of $\text{MoSe}_2 @\text{NC}@r\text{GO}$; (b) SAED pattern; (c) cycling performances; (d) rate performances under different current densities; (e) cycling performances at 1 A g^{-1} ; (f) a schematic diagram of $\text{MoSe}_2 @\text{NC}@r\text{GO}-200$ full cell; (g,h) electrochemical performance of the full cell [80].

Alternatively, metal–organic frameworks grown directly on the surface of electrode materials and then annealed can also be clad. Metal–organic frameworks (MOFs) are generally porous irregular polyhedra with high porosity, large specific surface area, and tunable topology [86]. When TMX nanoparticles are annealed with MOFs, the nanoparticles can be encapsulated in the carbon matrix formed by MOFs, and the MOF morphology can be maintained. The unique MOF structure can improve the stability of the material structure due to its nano-size and high porosity. Zhao’s research group [87] mixed and annealed the Co-based zeolite imidazole acid framework (ZIF-67) with thioacetamide. Thioacetamide was transformed into Co_9S_8 and embedded in the polyhedron ZIF-67. The organic ligand of ZIF-67 was transformed into a porous carbon layer and coated on the surface of the composite, forming a rigid porous yolk-shell structure. It still shows excellent electrochemical performance after 800 cycles [87]. However, MOF precursors are prone to aggregation during repeated charge/discharge cycles, and the design of MOFs with hierarchical structures may be a promising solution. Zhou’s research group [88] obtained hierarchical flower-like zinc–manganese binary selenide ZMS@FC composed of multiple flakes by solvent thermal self-assembly, and the tight coupling between the metal selenide and carbon matrix makes the hierarchical structure extremely stable, in which the zinc–

manganese binary selenide nanoparticles are uniformly anchored on 2D porous carbon sheets. The existence of porous carbon sheets inhibits the volume change in active materials in the cyclic process and limits the size of the nanoparticles, especially a large number of mesoporous structures at the cross-section of petals, which dramatically improves the electrolyte penetration and electron transfer efficiency and achieves excellent long-cycle stability in SIBs ($369.6 \text{ mA h g}^{-1}$ at 2 A g^{-1} after 1000 cycles) [88].

The cladding mentioned above is often performed in simple systems with smooth surfaces, and it would be challenging to clad complex materials with particles on the surface using the previous method. Yousaf's research group [89] adopted a simple three-step approach to grow FeSe_2 nanoparticles on the surface of carbon nanotubes and form amorphous carbon layers (Figure 6a). TEM and HRTEM images (Figure 6b,c) showed that this method not only wraps the carbon layer on each carbon nanotube but also coated the FeSe_2 nanoparticles on the carbon nanotube with a layer of amorphous carbon, achieving the double cage protection of FeSe_2 nanoparticles. When used as the negative electrode for SIBs, it exhibits excellent electrochemical performance (Figure 6d–f) [89].

3.2. Enhanced Conductivity of Electrodes

The TMX band gap is relatively narrow, and when the band gap is narrowed to a certain extent, it exhibits metal-like behavior, which means that the material may have high electrical conductivity [16]. Nevertheless, because most TMXs are semiconductor materials, and the number of free electrons and holes in semiconductors is minimal, they face the problem of relatively poor electrical conductivity in practical applications. To solve the problem of relatively poor conductivity of electrode materials, researchers have proposed some solutions to improve the conductivity of electrodes, such as defect engineering, building heterogeneous structures, and compounding with carbonaceous materials.

3.2.1. Defective Engineering

Doping can change the distribution of holes and free electrons in semiconductor materials, while heteroatoms embedded in the lattice structure can introduce defects, increase dislocations, make the ion diffusion channel larger, and enhance the conductivity [90]. Essentially, electrons are pulled out of π -occupying orbitals or added to π -vacancy orbitals to reduce the energy level difference between adjacent orbitals, thereby increasing the electrical conductivity. Commonly used doping atoms are N, S, P, B, and other more polar non-metallic atoms. Among them, N and S doping are mainly used to modulate the electronic properties of carbon materials so that the electron pair polarization creates more active sites [91]. As the smallest and most electronegative atom in conventional dopants, the N atom is currently the most commonly used element in the heteroatom doping strategy, which can improve conductivity and wettability. In addition, N doping can generate defects and active sites that enhance the interfacial adsorption of the material, thus significantly improving the cycling performance [91]. Ge's research group [19] thoroughly ground Prussian blue with Se and then used the annealing treatment, and the inorganic ligand of Prussian blue was transformed into an N-doped carbon matrix uniformly encapsulated on the rod-like FeSe_2 surface. The N-doped carbon layer enabled it to exhibit excellent cycling stability. N doping can also be performed by annealing TMX nanomaterials with MOFs, in which a part of an MOF is formed in situ to cover the active substance with the carbon matrix, and the other part becomes N doped in the carbon matrix. This method is more direct and convenient [19]. Jiang's research group [92] first self-assembled ZIF-67 polyhedra on the graphene surface and then transformed ZIF-67 into hollow polyhedral CoSe with N-doped carbon by selenization heat treatment, which provided a significantly better high-rate capacity of 290 mAh g^{-1} at 5 A g^{-1} than bare CoSe when used as an SIB anode.

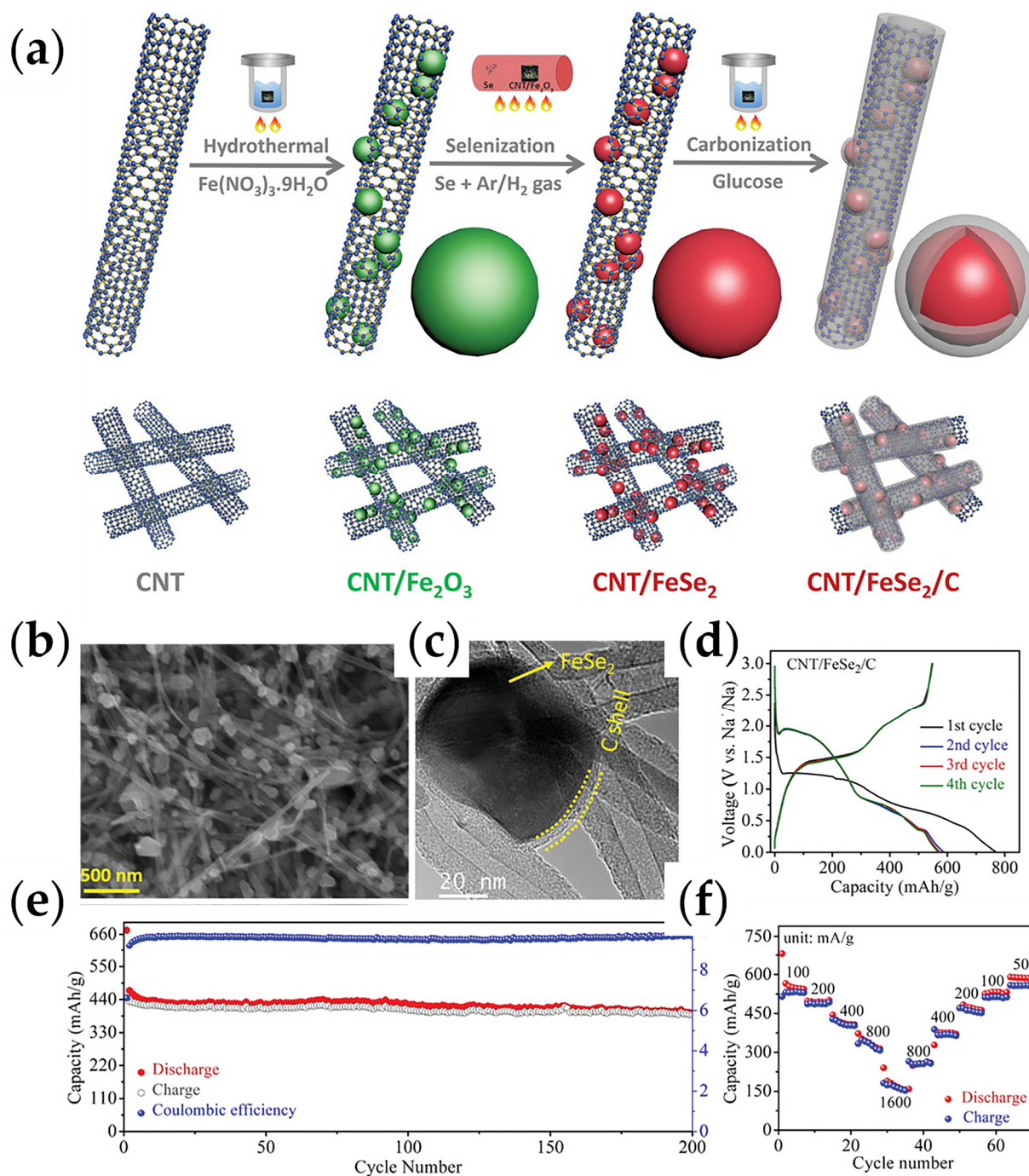


Figure 6. (a) The fabrication process of the CNT/FeSe₂/C and (b) CNT/FeSe₂/C frameworks, respectively; (c) low magnification of TEM; (d–f) electrochemical performance of CNT/FeSe₂/C [89].

Sulfur doping also improves the hydrophilicity of the surface carbon material and facilitates charge transfer at the electrolyte, electrode, and interface. Yang's research group [93] grew CoSn(OH)₆ in situ on graphene oxide by the co-precipitation method and then obtained S-doped graphene oxide/(SnCo)S₂ nanocube heterostructures by direct vulcanization. The sulfur doping, graphene oxide coating, and the formation of the heterostructure make it have outstanding electrochemical properties [93]. Phosphorus doping is also a good choice not only to introduce defects to enhance the ion diffusion kinetics and enhance the electrical conductivity of the material but also to form stronger P–M bonds than P–S/Se bonds (M is a transition metal), improving the structural strength of the mate-

rial [94–96]. Ma's research group [97] obtained carbon skeleton-coated P-doped Cu_2Se hollow nanospheres rich in Se vacancies by phosphorylating dopamine-coated tetragonal phase Cu_2Se nano hollow spheres, which have long cycle stability (over 95% capacity retention for 1000 cycles) at an ultra-high current density of 20.0 A g^{-1} .

Diatomic doping generally can achieve better electrochemical properties than single-atom doping due to the synergistic effect. Niu's research group [98] obtained supramolecular aggregates by reacting melamine and phytic acid at room temperature and depositing them on the surface of graphene oxide as a framework for the growth of MoSe_2 . Finally, the supramolecular aggregates were decomposed into N and P by high-temperature calcination and co-doped on the surface of graphene oxide to obtain MoSe_2/N , P-rGO. The N and P co-doping synergies lead to better electrical conductivity, fast charge transfer kinetics, and increased pseudocapacitance contributions. N and P co-doping results in good electrochemical performance, but the previously used N and P dopants are generally expensive and pollute the environment. Chlorella has the advantage of being abundant, cheap, and rich in N and P elements, and is expected to be a new N and P co-dopant [98]. Xu's research group [99] embedded spherical V_3Se_4 in carbon nanofibers by electrospinning technology, and chlorella provided N and P elements to be doped in the carbon nanofiber matrix and finally obtained a $\text{V}_3\text{Se}_4/\text{NPCNFs}$ composite with a good capacity of 240 mAh g^{-1} after 13,000 cycles at 10 A g^{-1} .

The formation of vacancies is also related to the introduction of heteroatoms; for example, when trivalent nitrogen atoms are doped with tetravalent carbon atoms, due to the formation of only three covalent bonds, the carbon atoms will capture electrons from the surrounding area and cause a net surplus of positive charge, resulting in vacancies. At the same time, the formation of vacancy defects will increase the active sites, improve the transfer of electrons and Na^+ , and facilitate the storage of Na^+ [74]. At the same time, the formation of vacancy defects increases the active sites, improves electron and ion transfer, and facilitates sodium ion storage. For example, the carbon-coated P-doped Cu_2Se hollow nanospheres rich in Se vacancies prepared by Ma's research group [97] exhibited excellent capacity and long-cycle stability when used as an SIB anode. Vacancies can also be introduced by the partial elimination of sulfur or selenium from TMXs using redox reactions. Ma's research group [100] prepared MoS_2/C composites by hydrothermal reaction and high-temperature carbonization and reduced the sulfur atoms in MoS_2 to H_2S using a strong reducing agent hydrazine hydrate to remove the sulfur atoms to obtain a range of MoS_2/C material with various sulfur vacancy concentrations (Figure 7a). Transmission electron microscopy (TEM) images (Figure 7b) show the ultra-thin layer morphology of the MoS_2/C composites, which avoids the agglomeration of multilayer MoS_2 materials. The electron paramagnetic resonance (EPR) spectra (Figure 7c) can be obtained with the increase in the amount of hydrazine hydrate and the increase in the S vacancy concentration. The density of states (DOS) figure shows that the gap of sulfur-containing vacancy material is smaller, and the conductivity is higher when comparing the sulfur-containing and sulfur-free vacancies (Figure 7d). Finally, after combining the binding energy and embedding energy and volume change before and after Na^+ adsorption of Na^+ samples with diverse concentrations of sulfur vacancies, it can be concluded that sulfur vacancies at 12.5 to 18.75% atomic concentration can improve the electrical conductivity without affecting the volume change (Figure 7e). Electrochemical performance as shown in Figure 7f,g [100].

3.2.2. Construction of Heterogeneous Structures

When two materials with different Fermi energy levels come into contact, the interface structure is called a heterojunction, and a multilayer heterojunction is called a heterostructure. The difference in Fermi energy levels allows the presence of a built-in electric field at the heterogeneous interface, which significantly accelerates the charge transfer process and thus enhances the electrical conductivity of the material [101]. The standard methods to construct heterostructures include mechanical assembly and the in situ growth of components combined with chemical bonding forces. In general, in situ development consists

of one component growing directly on a specific crystal plane of another component, and the resulting heterostructure is more robust. For TMXs, the in situ growth method of chemical vapor deposition is commonly used to construct heterogeneous structures. This method also has the advantage of regulating the configuration of heterogeneous structures by controlling synthetic parameters (gas flow rate and temperature). Wei's research group [54] prepared FeS nanowires (FeS@NSC composite) uniformly coated with N and S co-doped carbon layers by a simple one-step chemical vapor deposition method and formed heterostructures with solid interaction on the surface of ultra-thin carbon shell and FeS nanowires. This method has better environmental compatibility, good cost effect, and a simpler procedure than previous synthesis methods. When used as an SIB anode, it exhibits high capacity ($611.6 \text{ mA h g}^{-1}$) and excellent long-cycle stability (94.7% capacity retention after 2000 cycles at high current density 20 A g^{-1}) [54].

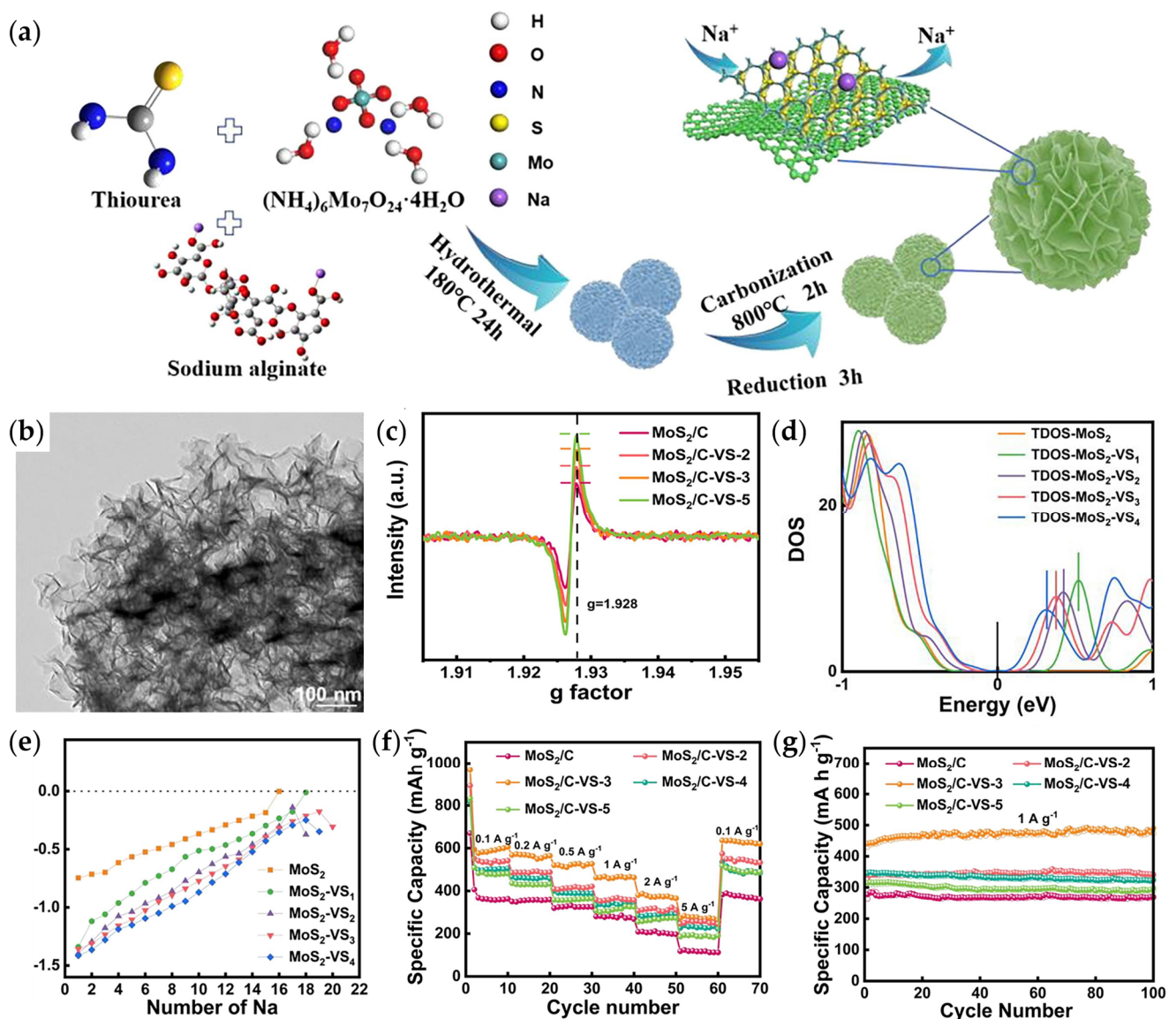


Figure 7. (a) A sketch of the preparation of MoS_2 with S-vacancies; (b) TEM; (c) EPR results; (d) density of states; (e) intercalation energy of Na^+ ; (f,g) electrochemical performance [100].

Although the heterostructure constructed by TMXs and traditional carbon-based materials can indeed enhance the electrochemical performance, due to the poor electronic coupling between non-polar carbon materials and polar TMXs, the formed heterostructures are challenging for maintaining structural stability for a long time and ultimately hinder

the rapid transfer and diffusion of ions, resulting in reduced cycling performance [102–104]. The strongly polar MXene has more substantial electrical conductivity and lower ion migration potential than the conventional carbon materials, and there are also a large number of O, OH, F, and other functional groups on the surface to regulate the interfacial properties, which are expected to replace the conventional carbon materials and TMXs to form MXene-based heterostructures with better performance [105,106]. However, synthesizing such heterostructures is not only tedious but also uses strong corrosive HF, and even the oxidation of HF may lead to the oxidation of MXene, which significantly hinders the broad application of this heterostructure. To address this problem, Huang's research group [107] developed a simple and safe molten salt etching method to successfully prepare $\text{Ti}_3\text{AlC}_2/\text{MS}_y$ heterostructures, which is generally applicable to other TMXs. The authors first redox the MAX precursor Ti_3AlC_2 with $\text{FeCl}_2 \cdot 4\text{H}_2\text{O}$ molten salt by molten salt etching, where Fe^{2+} oxidized the Al in Ti_3AlC_2 to Al^{3+} away, leaving the gaps connected by functional groups such as Cl, OH, O, etc. (Figure 8a). Since these functional groups contain lone pairs of electrons and can adsorb transition metals containing empty orbitals, the $\text{Ti}_3\text{C}_2\text{T}_x/\text{MS}_y$ heterostructure is finally obtained by sulfidation treatment. This method avoids hazardous HF and the oxidation of MXene due to the synthesis in a molten salt environment. In addition, TMXs are grown in situ on MXene, and the interface between the two exhibits a strong interfacial electron coupling effect, ensuring close contact between $\text{Ti}_3\text{C}_2\text{T}_x$ and FeS_2 . When the $\text{Ti}_3\text{C}_2\text{T}_x/\text{FeS}_2$ heterostructure is used as the SIB anode, the dual sodium storage mechanism results in excellent rate performance (Figure 8b) and outstanding long-cycle stability (Figure 8c). In addition, the sodium ion full cell assembled from the $\text{Ti}_3\text{C}_2\text{T}_x/\text{FeS}_2$ -negative electrode and the $\text{Na}_3\text{V}_2(\text{PO}_4)_3$ cathode has an outstanding specific capacity of 431.6 mAh g^{-1} after 1000 cycles at 3 A g^{-1} . In conclusion, generating highly conductive $\text{Ti}_3\text{C}_2\text{T}_x$ MXene with a heterogeneous TMX interface exhibits significantly enhanced electron conductivity, Na^+ diffusion kinetics, and robust structure (Figure 8d) [107].

Additionally, TMXs with metal monomers to form heterostructures are also a good choice. Compared with the poor bulk energy of TMX/conducting nanocarbon heterostructures, TMX/metal monomers may achieve both fast electron/ion transport and high-volume capacity. Sun's research group [108] generated Ni- Ni_3S_2 @SC composites in situ on mesoporous NiO templates using one-step chemical vapor deposition (CVD) and thiophene reduction. Here, the thiophene not only provided the sulfur source but also partially transformed into a dense S-doped carbon matrix coating the NiO surface of the internal interconnected pore channels, and the presence of carbon reduced a small quantity of NiO to Ni nanoparticles modified on the Ni_3S_2 nanoparticle surface, resulting in two heterogeneous interfaces $\text{Ni}_3\text{S}_2/\text{carbon}$ and $\text{Ni}/\text{Ni}_3\text{S}_2$. The dense S-doped carbon matrix coating ensured the stability of the structure, and the Ni nanoparticles promoted internal electron transport. The construction of two heterogeneous interfaces provides a strong electric field to enhance the electron conductivity and ion migration kinetics, resulting in Ni- Ni_3S_2 @SC composites with good rate performance, extended cycle stability, and high volume capacity for both potassium ion batteries and SIB applications [108]. When two TMXs have similar lattice structures and suitable energy band gap differences, electrons can be transferred between different energy levels and thus form a heterostructure [109]. Zhang's research group [110] prepared a dense, non-porous $\text{Fe}_9\text{S}_{10}@\text{MoS}_2@\text{C}$ composite material with Fe_9S_{10} as the core and sequenced MoS_2 and carbon coating on the surface. This dense (1.27 g cm^{-3}) non-porous structure possesses an incomparable vibrational density of previous materials. Due to the vast energy band gap between the highly conductive Fe_9S_{10} and MoS_2 , a solid electric field heterostructure is formed, which enables it to undergo fast ion diffusion kinetics, even in a dense structure [110].

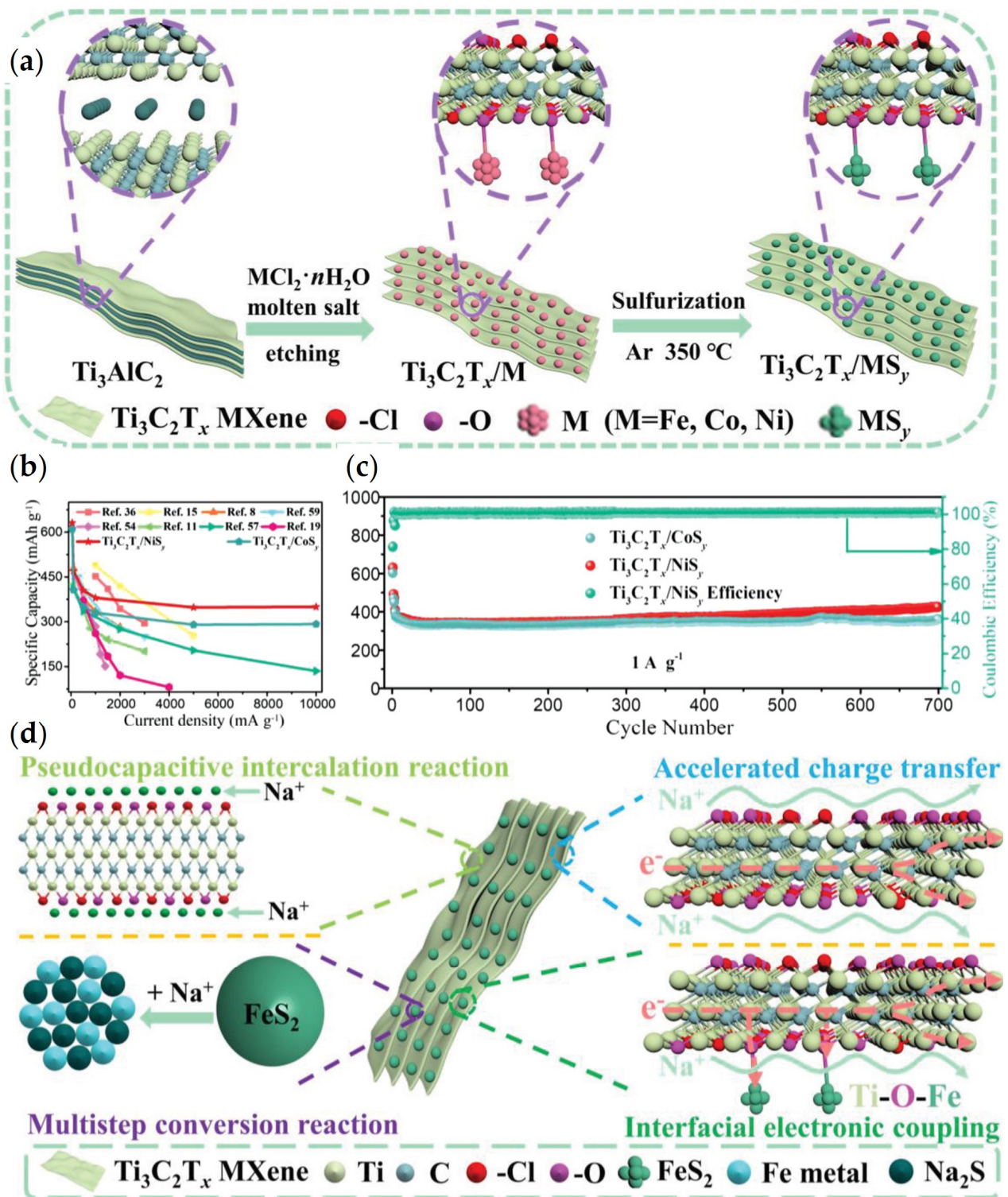


Figure 8. (a) A schematic diagram of the synthetic process of $\text{Ti}_3\text{C}_2\text{T}_x/\text{MS}_y$; (b) comparison of rate performance; (c) long-term cyclic performance; (d) sodium storage mechanism [107].

During the Na-ion insertion/extraction in TMXs, transition metal and NaX_n are often formed by conversion reactions. However, due to the agglomeration of the intermediate product NaX_n , the reversibility of the conversion reaction is affected, resulting in slow sodium ion transport kinetics. It is inferred that the built-in electric field often formed by the heterostructure, especially when the other phase constituting the heterostructure is non-

homogeneous, produces a phase interface that induces lattice defects and deformations at the heterostructure interface, which can eventually improve the Na^+ storage energy [76,77]. Cao's research group [111] briefly prepared $\text{Bi}_2\text{S}_3/\text{MoS}_2$ heterostructures and explored in depth how the phase interfaces generated by the non-homogeneous heterostructures can improve the sodium ion storage kinetics. First, the authors observed that TEM and HRTEM images can obtain the non-homogeneous structure and multiphase morphology of the complexes. Here, the non-homogeneous heterostructures are formed spontaneously because Bi_2S_3 is a P-type semiconductor with positively charged hole conductivity, and MoS_2 is an N-type semiconductor with electron conductivity. Heterojunctions are easily created when the two semiconductor materials have different forbidden bandwidths. The reasonable construction of the heterostructure generates abundant phase boundaries, increases the storage sites of Na^+ , improves the electronic conductivity, and enables the recrystallization and homogeneous distribution of the agglomerated intermediate product NaX_n so that the conversion reactions of Bi_2S_3 and MoS_2 with Na^+ can be carried out reversibly, which enhances the stability of the structure and finally shows excellent sodium storage capacity [111].

3.2.3. Composite with Carbonaceous Materials

It is a standard method to compound TMXs with a highly conductive carbon material to improve the conductivity of the electrode. The introduction of the carbon material can provide a directional transport channel for ions and electrons, thus speeding up the dynamics and reducing the transmission resistance. In addition, it can also separate the nanomaterials to ease the aggregation and reserve buffer space for the volume change [112–114]. Antimony-based materials have high theoretical capacity, but low conductivity and significant volume expansion limit their applications. Yang's research group [115] successfully prepared Sb_2X_3 ($\text{X}=\text{S}$ or Se) nanodots confined within S- or Se-doped conductive carbon skeletons by sulfidation or selenization using antimony sodium gluconate as the precursor, where each nanodot is protected by an interconnected carbon network, and both improve conductivity and mitigate volume expansion. In addition, the ultra-small nanodots also provide smaller Na^+ diffusion energy barriers and shorter sodium ion transport channels [115].

Heteroatom doping can induce structural distortions and charge density changes in carbon materials, providing a large number of active sites. Therefore, doping heteroatoms in carbon materials can improve the electronic and chemical properties of regulated carbon materials, and the electrical conductivity of the materials will be better [116,117]. Sun's research group [118] calcined the precursor $\text{ZnSn}(\text{OH})_6$ coated with polydopamine at a high temperature, in which the polydopamine becomes an N-doped carbon shell encapsulated on the surface of the precursor. At the same time, the zinc evaporates, leaving voids. Finally, the cubic block of N-doped carbon shells encapsulated with spherical SnS_2 nanoparticles of $\text{SnS}_2@\text{C}$ yolk-shell composites is obtained by sulfidation treatment. Voids exist between the carbon shells and the SnS_2 core. The formation of the N-doped carbon shell prevents the aggregation of SnS_2 nanoparticles, relieves the volume expansion, and forms a conductive carbon matrix to increase the electrical conductivity of the material. When used as an SIB anode, it exhibits excellent specific capacity (750 mAh g^{-1} at 100 mA g^{-1}) [118].

Graphene with large π bonds of multiple atoms has excellent electrical conductivity and is commonly used as a carbonaceous network. Mainly, TMXs with a high specific surface area can produce a large interface area when coupled with graphene, significantly shortening the ion diffusion path and forming a highly accessible channel at the interface, which promotes the formation of surface redox pseudocapacitors and interfacial pseudocapacitors, respectively. Graphene oxide (GO) is the oxidized graphene, which is more active than graphene with wealthy oxygen-containing functional groups [119]. However, the direct coupling is complex due to the electrostatic repulsion between the oxygen-containing functional groups and oxide precursors on graphene oxide, and the electrostatic charge on the surface of graphene oxide needs to be adjusted first [120–122]. Zhao's research

group [123] used the surfactant cetyltrimethylammonium bromide (CTAB) to assist in coordinating the surface charge of graphene oxide. The long-chain alkyl part of CTAB is connected to the GO surface, and the positively charged CAT^+ attracts the MoO_4^{2-} anion, which uses the strong interfacial coupling formed by the Mo-C chemical bond to prepare MoSe_2 nanosheets with directionally controlled growth on graphene. Here, the graphene matrix effectively prevents the aggregation of MoSe_2 nanosheet arrays and enhances the conductivity of the electrode [123].

Another method is the composite with MOF precursors, where the carbon matrix and metal ions come from the same molecule. The two will be more tightly bonded in the subsequent process, effectively overcoming the drawbacks of the external carbon source. Li's research group [124] embedded ultra-small Fe_7S_8 nanoparticles into the N-, S-, and O-doped carbon skeleton to obtain $\text{Fe}_7\text{S}_8@HD\text{-C}$ composite material. The heteroatom-doped carbon skeleton provides a conductive path for electroactive particles, promotes the rapid transfer of sodium ions, and improves the conductivity, showing excellent reversible capacity of sodium ion storage (0.1 A g^{-1} , 675 mAh g^{-1}) [124]. Zhao's research group [125] used polyacrylonitrile (PAN) nanofibers obtained by electrospinning technology as the skeleton and then grew cobalt organic framework (ZIF-67) nanofibers vertically on PAN nanofibers by a simple liquid-phase impregnation growth method, and obtained "dendritic" CNF@CoSSe@C by selenization treatment. This bionic design results in a suitable electronic structure, low Na^+ migration barrier during charging and discharging, and excellent electrical conductivity, and exhibits excellent long-cycle stability (over 13,000 cycles at 20.0 A g^{-1} with a capacity decay rate of 0.01%) when CoSSe@C is used as an SIB anode [125].

MXene is a graphene-like structure obtained by etching the A element in the MAX phase (M is the transition metal of the previous groups, A is the leading group element, and X is C or N), which often exhibits excellent metal-like electrical conductivity (up to $\sim 10^4 \text{ S cm}^{-1}$) due to the combination of MXene surface, which may be pretty complex with one or some hydroxyl groups, O, F, and other capping groups [126,127]. Li's research group [128] grew ZIF-67 polyhedrons on the hollow thin-walled spherical MXene surface in situ and then obtained N-doped carbon-coated CoS_2 nanoparticles ($\text{MXene@CoS}_2/\text{NC}$) on the hollow thin-walled spherical MXene surface in situ by subsequent carbonization and sulfurization. Here, MXene provides high electrical conductivity and ion transport channels. The hollow spherical structure can relieve volume expansion, and the construction of CoS_2 and MXene heterostructures can modulate the Co-S bond energy and improve the sodium storage kinetics of CoS_2 . When used as an SIB anode, $\text{MXene@CoS}_2/\text{NC}$ exhibits high reversible capacity (620 mAh g^{-1} at 0.2 A g^{-1}), excellent rate performance (394 mAh g^{-1} at 5 A g^{-1}), and excellent cycling stability (355 mAh g^{-1} after 5000 cycles) [128].

4. Conclusions

This paper briefly describes the main challenges encountered by TMXs in recent years for SIB-negative electrodes and the corresponding solution strategies, including nanostructure engineering, defect engineering, cladding engineering, the construction of heterostructures, and composites with carbonaceous materials. A summary of some of these solution strategies in recent years is presented in Table 1. Although these strategies have achieved good results so far, the capacity obtained is still far from the high theoretical capacity of TMXs, and many problems still need to be further investigated. According to our analysis, the future research directions of SIBs are prospected.

1. Mitigating the volume expansion and agglomeration of TMX materials during charge/discharge cycles is a crucial issue in improving structural stability. At present, the research mainly focuses on the structural and dimensional design of materials, apparently starting with the construction of small-sized nanomaterials, hollow structures, porous structures, and egg yolk-shell structures; these structures with void spaces are often constructed using MOF and MXene as templates, and the existence of voids can alleviate the volume change. The problem of small-size nanoparticles prone to accumulation and agglomeration can be alleviated by covering the surface of each

nanoparticle with carbon layers or carbon networks. The intrinsic aspect is mainly to regulate the crystal structure inside the material, and defects or vacancies are introduced by defect engineering to regulate the electron distribution, which in turn affects the crystal structure.

2. Enhancing the conductivity of materials is the key to obtaining high-capacity batteries, and most of the solutions commonly used at present focus on heteroatom doping, introducing vacancy, constructing heterogeneous structures, and composite with carbon matrix materials (such as graphene, MOF precursors, MXene, etc.). Traditional heteroatom doping such as N, S, P, and other atoms can also improve the conductivity of the materials, but such dopants are often more expensive and environmentally unfriendly. The use of cheap and environmentally compatible materials (such as chlorella) may be the future trend of dopant development. Building heterogeneous structures is also a common method to improve the conductivity of TMXs because it can form an internal electric field. The key to this approach is the choice of another material. For example, TMXs combined with a non-polar carbon material will form an unstable heterogeneous structure due to poor electronic coupling but can form a strong and stable electric field with a strongly polar carbon material (such as MXene). The volume energy of TMXs is often poor after forming a heterogeneous structure with conductive carbon, which can be solved by combining with metal elements/metal compounds. In addition, the formation of heterogeneous structures can also play a role in slowing down the agglomeration of intermediate products during the charge–discharge cycle. The development of materials that can form strong and stable heterogeneous structures with TMXs and have high-volume energy may be the trend of future development. Composite TMXs with carbonaceous materials (such as graphene oxide, MOF, MXene, etc.) are also a good choice, especially when using MOF materials, as the carbon matrix and metal ions are derived from the same molecule, and the two can form strong electronic coupling. Therefore, the development of carbon materials with strong electrical conductivity and strong electron coupling is the key to this method.
3. The current trend is to combine these approaches to improve structural stability and electrical conductivity and develop simpler, environmentally friendly, and less costly synthetic methods to synthesize TMX composites. In addition, it is necessary to combine more advanced characterization techniques and more theoretical work to fully explore the internal mechanism leading to the structural instability and poor electrical conductivity of active materials and fully understand the sodium storage mechanism and failure mechanism of SIBs. In recent years, full batteries that match TMX-negative electrodes with other positive electrode materials have been developed, but truly commercialized full batteries are few and far between and still require a lot of effort.

Table 1. Electrochemical performance of representative SIB anodes.

Materials	Synthesis Method	Cycle Performance	Rate Performance	Electrolyte	Voltage Interval	Reference
Fe ₇ Se ₈ @C@MoSe ₂	co-precipitation	87%/600/1	274.5/5	1M NaPF ₆	/	[129]
Willow-leaf-like ZnSe@NC	solvothermal	242.2/3200/8	144.4/10	1M NaCF ₃ SO ₃	0.01–3	[130]
FeSe ₂ @C microspheres	hydrothermal	428/1000/1	/	1M NaCF ₃ SO ₃	0.5–2.9	[131]
FeSe ₂ /NC@GE	/	323/1000/2	331/5	1M NaClO ₄	1.0–3	[132]
SnSe ₂ /ZnSe@PDA nanobox	co-precipitation	616/1000/1	/	1M NaPF ₆	0.1–3	[83]
FeSe ₂ @NC microrods	hydrothermal	401.3/2000/5	411/10	1M NaCF ₃ SO ₃	0.4–2.9	[133]
ZnSe@N-C@MoSe ₂ /rGO	template engaged	177.7/5000/10	224.4/10	1M NaClO ₄	0.01–3	[134]

Table 1. Cont.

Materials	Synthesis Method	Cycle Performance	Rate Performance	Electrolyte	Voltage Interval	Reference
Mesoporous FeSe ₂ @C	selenization	483/100/0.2	/	1M NaClO ₄	0–3	[135]
Core/shell FeSe @CNS nanosheet	in situ pyrolysis	100/10,000/30	183.8/30	1M NaCF ₃ SO ₃	0.01–2.8	[136]
CNT/FeSe ₂ /C	wet chemistry	546/100/0.1	423/0.5	1M NaClO ₄	0.01–3	[89]
Fe ₇ Se ₈ /N-CNF	electrospinning	/	286.3/20	1M NaCF ₃ SO ₃	0.5–2.5	[78]
SnSe ₂ /FeSe ₂ /NC	co-precipitation	408.1/1200/6	345/20	1M NaPF ₆	/	[137]
CoSe/G	self-assembly	214/600/2	290/5	1M NaClO ₄	0.01–3	[92]
In ₂ Se ₃ -CoIn ₂ -CoSe ₂	/	205.5/2000/10	371.6/20	1M NaPF ₆	0.01–2.5	[138]
FeSe ₂ microspheres	solvothelmal	/	525/20	1M NaPF ₆	0.01–3	[139]
FeSe ₂ @rGO	/	350/600/5	/	1M NaPF ₆	0.01–3	[140]
Co _{0.85} Se@ carbon nanotubes	pyrolysis selenization	306.4/800/2	222.5/5	1M NaClO ₄	/	[75]
Rich-oxygen-doped FeSe ₂ nanosheets	/	268/700/1	258/3	1M NaCF ₃ SO ₃	0.25–2.5	[141]
3DG/CoSe ₂ @CNWs	solvothelmal	302/500/2	/	1M NaClO ₄	0.01–3	[64]
VSe ₂ @PPy	selenization	324.6/2800/4	260/10	1M NaPF ₆	/	[142]
Bi ₂ S ₃ /MoS ₂	solvothelmal	323.4/1200/10	/	1M NaCF ₃ SO ₃	0.1–3	[111]
Fe ₇ S ₈ @HD-C	one-step sulfidation	480/320/2	326/10	1M NaPF ₆	0.01–3	[124]
Cu _{1.81} S truss structures	selective reduction	77.7%/1000/3	331/3	1M NaPF ₆	0.01–2.6	[65]
SnS ₂ @C nanobox	metal evaporation	/	362/5	1M NaClO ₄	0.01–2.5	[118]
Hollow CuS	hydrothelmal	/	246.4/5	1M NaCF ₃ SO ₃	0.001–3	[143]
Fe ₉ S ₁₀ @MoS ₂ @C	/	93.4%/1000/2	132/50	1MNaClO ₄	/	[110]
Nb ₂ CT _x @MoS ₂ @C	hydrothelmal	403/2000/1	260/40	1M NaClO ₄	0.01–3	[58]
CuS/FeS ₂ @NC	two-step pyrolysis	99.1%/300/5	537/5	1M NaPF ₆	0.01–2.7	[144]
Hollow MXene@CoS ₂ /NC	carbonization and sulfurization	620/5000/0.2	394/5	1M NaCF ₃ SO ₃	0.25–3	[128]
Lotus-leaf-like FeS @N, S-CNSs	construction	370/300/5	/	1M NaSO ₃ CF ₃	0.02–2.5	[145]
GeTiS ₃	atomic scissors	209/10,000/32C	209/32C	1M NaPF ₆	0.01–2.5	[146]
Ni-Ni ₃ S ₂ @SC	edge-to-edge	/	289/2	1M NaClO ₄	0.01–3	[108]
Yolk-shell Fe ₇ Se ₈ @C/N nanoboxes	etching and selenization	Nearly 100%/1000/1	316/5	1M NaCF ₃ SO ₃	0.5–2.5 V	[147]
Few-layered Ti ₃ C ₂ /Co ₂ Se ₄	solvothelmal	379.2/100/0.1	289.1/5	1M NaClO ₄	0.01–3	[148]
V ₃ Se ₄ /NP CNFs	electrospinning	340/8000/5	240/113,000/10	1M NaClO ₄	0.01–3	[99]
Fe ₃ Se ₄ /ZnSe@C	/	473.8/300/5	456.2/5	1M NaCF ₃ SO ₃	0.01–3	[149]
Co ₃ Se ₄ @rGO	selenization	/	229.3/50	1M NaClO ₄	0.01–3	[150]
Cu ₂ P _x Se _{1-x} @C	/	249.7/1000/20	/	1M NaCF ₃ SO ₃	0.01–3.0	[97]
Co _{0.85} Se-Fe ₇ Se ₈ @rGO	/	300.8/1000/1	/	1M NaPF ₆	0.01–3.0	[151]
Cu ₂ Se@PPy	self-polymerization	263.5/2000/10	/	1M NaCF ₃ SO ₃	/	[152]
Branch-leaf CNF@CoSSe@C	electrospinning	0.01%every cycle/13,000/20	/	1M NaCF ₃ SO ₃	0.01–3.0	[125]
Fe ₃ Se ₄ @SiO ₂ @C nanorods	situ conformal growth	272/4200/20	/	1M NaCF ₃ SO ₃	/	[153]
NiTeSe–NiSe ₂ nanotubes	hydrothelmal	389.6/1400/10	582.5/0.5	1M NaPF ₆	0.01–3	[154]
NiSe ₂ @NGCF	template	406.1/3000/5	558.3/200/0.5	1M NaClO ₄	0.01–3	[155]

Table 1. Cont.

Materials	Synthesis Method	Cycle Performance	Rate Performance	Electrolyte	Voltage Interval	Reference
V ₂ C/Fe ₇ S ₈ @C composites	hydrothermal	/	389.7/5	1M NaClO ₄	0.01–3	[156]
SnS/SnS ₂ @SG-K	alkali ion-assisted growth	372/500/10	241/0.05/48	1M NaClO ₄	0.01–3	[157]
CuGaSe ₂ @ZnSe-NC	hydrothermal	276/2000/2	595/0.2	1M NaClO ₄	0.01–3	[158]
CoSe ₂ /O-C	salt-fixed and thermochemical manners	346/3500/15	/	1M NaCF ₃ SO ₃	0.01–3	[159]
SnS _{1.5} Se _{0.5} /NS-C	microwave	670/500/0.2	647/10,000/5	1M NaPF ₆	0.5–2.8	[160]
NiSe ₂ /CoSe ₂ nanoparticles	solvothermal co-precipitation	296.4/1500/10	296.4/10	1M NaCF ₃ SO ₃	0.01–3	[161]
SnSe _{0.5} S _{0.5} @NG	in situ encapsulating	547/200/0.2	387/10	1M NaClO ₄	0.01–3	[162]
Ni _{1/3-x} Co _{1/3-y} Mn _{1/3-z} Se ₂ /MnSe ₂	co-precipitation and high-temperature solid-state route	400/2000/2	400/2	1M NaPF ₆	0.3–3	[163]

Author Contributions: Writing—review and editing, C.W., D.Q. and Q.L.; supervision, Z.S. (Zhonghui Sun), Z.S. (Zhongqian Song); resources, H.G. and L.N. All authors have read and agreed to the published version of the manuscript.

Funding: This work is financially supported by the National Natural Science Foundation of China (22204028, 22104021, 22204159), the Young Talent Support Project of Guangzhou Association for Science and Technology (QT-2023-003), the Guangdong Basic and Applied Basic Research Fund Project (2022A1515110451), the Guangzhou University Graduate Student Innovation Ability Cultivation Funding Program (2022GDJC-M06), and the Science and Technology Projects in Guangzhou (202201010245, 2023A03J0029).

Data Availability Statement: Not applicable.

Conflicts of Interest: The authors declare no conflict of interest.

References

- Gu, R.; Ma, Z.; Cheng, T.; Lyu, Y.; Nie, A.; Guo, B. Improved Electrochemical Performances of LiCoO₂ at Elevated Voltage and Temperature with an In Situ Formed Spinel Coating Layer. *ACS Appl. Mater. Interfaces* **2018**, *10*, 31271–31279. [CrossRef] [PubMed]
- Yang, X.; Rogach, A.L. Anodes and Sodium-Free Cathodes in Sodium Ion Batteries. *Adv. Energy Mater.* **2020**, *10*, 2000288. [CrossRef]
- U.S. Geological Survey (USGS). *Mineral Commodity Summaries 2020*; U.S. Geological Survey (USGS): Reston, VA, USA, 2020; p. 204.
- Li, Y.; Feng, X.; Ren, D.; Ouyang, M.; Lu, L.; Han, X. Thermal Runaway Triggered by Plated Lithium on the Anode after Fast Charging. *ACS Appl. Mater. Interfaces* **2019**, *11*, 46839–46850. [CrossRef]
- Deng, W.-N.; Li, Y.-H.; Xu, D.-F.; Zhou, W.; Xiang, K.-X.; Chen, H. Three-dimensional hierarchically porous nitrogen-doped carbon from water hyacinth as selenium host for high-performance lithium–selenium batteries. *Rare Metals* **2022**, *41*, 3432–3445. [CrossRef]
- Yan, B.; Zheng, J.; Feng, L.; Zhang, Q.; Zhang, C.; Ding, Y.; Han, J.; Jiang, S.; He, S. Pore engineering: Structure-capacitance correlations for biomass-derived porous carbon materials. *Mater. Des.* **2023**, *229*, 111904. [CrossRef]
- Deng, W.; Xu, Y.; Zhang, X.; Li, C.; Liu, Y.; Xiang, K.; Chen, H. (NH₄)₂Co₂V₁₀O₂₈·16H₂O/(NH₄)₂V₁₀O₂₅·8H₂O heterostructure as cathode for high-performance aqueous Zn-ion batteries. *J. Alloys Compd.* **2022**, *903*, 163824. [CrossRef]
- Yan, B.; Feng, L.; Zheng, J.; Zhang, Q.; Jiang, S.; Zhang, C.; Ding, Y.; Han, J.; Chen, W.; He, S. High performance supercapacitors based on wood-derived thick carbon electrodes synthesized via green activation process. *Inorg. Chem. Front.* **2022**, *9*, 6108–6123. [CrossRef]
- Han, B.; Zou, Y.; Zhang, Z.; Yang, X.; Shi, X.; Meng, H.; Wang, H.; Xu, K.; Deng, Y.; Gu, M. Probing the Na metal solid electrolyte interphase via cryo-transmission electron microscopy. *Nat. Commun.* **2021**, *12*, 3066. [CrossRef]
- Luo, M.; Yu, H.; Hu, F.; Liu, T.; Cheng, X.; Zheng, R.; Bai, Y.; Shui, M.; Shu, J. Metal selenides for high performance sodium ion batteries. *Chem. Eng. J.* **2020**, *380*, 122557. [CrossRef]

11. Hwang, J.-Y.; Myung, S.-T.; Sun, Y.-K. Sodium-ion batteries: Present and future. *Chem. Soc. Rev.* **2017**, *46*, 3529–3614. [[CrossRef](#)]
12. Guo, X.; Zhang, W.; Zhang, J.; Zhou, D.; Tang, X.; Xu, X.; Li, B.; Liu, H.; Wang, G. Boosting Sodium Storage in Two-Dimensional Phosphorene/Ti₃C₂Tx MXene Nanoarchitectures with Stable Fluorinated Interphase. *ACS Nano* **2020**, *14*, 3651–3659. [[CrossRef](#)] [[PubMed](#)]
13. Hu, X.; Liu, Y.; Li, J.; Wang, G.; Chen, J.; Zhong, G.; Zhan, H.; Wen, Z. Self-Assembling of Conductive Interlayer-Expanded WS₂ Nanosheets into 3D Hollow Hierarchical Microflower Bud Hybrids for Fast and Stable Sodium Storage. *Adv. Funct. Mater.* **2020**, *30*, 1907677. [[CrossRef](#)]
14. Kang, H.; Liu, Y.; Cao, K.; Zhao, Y.; Jiao, L.; Wang, Y.; Yuan, H. Update on anode materials for Na-ion batteries. *J. Mater. Chem. A* **2015**, *3*, 17899–17913. [[CrossRef](#)]
15. Luo, W.; Shen, F.; Bommier, C.; Zhu, H.; Ji, X.; Hu, L. Na-Ion Battery Anodes: Materials and Electrochemistry. *Acc. Chem. Res.* **2016**, *49*, 231–240. [[CrossRef](#)] [[PubMed](#)]
16. Yang, T.; Fang, M.; Liu, J.; Yang, D.; Liang, Y.; Zhong, J.; Yuan, Y.-J.; Zhang, Y.; Liu, X.; Zheng, R.; et al. Ultranarrow Bandgap Se-Deficient Bimetallic Selenides for High Performance Alkali Metal-Ion Batteries. *Adv. Funct. Mater.* **2022**, *32*, 2205880. [[CrossRef](#)]
17. Ou, X.; Yang, C.; Xiong, X.; Zheng, F.; Pan, Q.; Jin, C.; Liu, M.; Huang, K. A New rGO-Overcoated Sb₂Se₃ Nanorods Anode for Na⁺ Battery: In Situ X-Ray Diffraction Study on a Live Sodiation/Desodiation Process. *Adv. Funct. Mater.* **2017**, *27*, 1606242.
18. Zhang, K.; Park, M.; Zhou, L.; Lee, G.-H.; Li, W.; Kang, Y.-M.; Chen, J. Urchin-Like CoSe₂ as a High-Performance Anode Material for Sodium-Ion Batteries. *Adv. Funct. Mater.* **2016**, *26*, 6728–6735. [[CrossRef](#)]
19. Ge, P.; Hou, H.; Li, S.; Yang, L.; Ji, X. Tailoring Rod-Like FeSe₂ Coated with Nitrogen-Doped Carbon for High-Performance Sodium Storage. *Adv. Funct. Mater.* **2018**, *28*, 1801765. [[CrossRef](#)]
20. Tang, W.; Xie, D.; Shen, T.; Wang, X.; Wang, D.; Zhang, X.; Xia, X.; Wu, J.; Tu, J. Construction of Nitrogen-Doped Carbon-Coated MoSe₂ Microspheres with Enhanced Performance for Lithium Storage. *Chem.-Eur. J.* **2017**, *23*, 12924–12929. [[CrossRef](#)]
21. Kwon, H.-T.; Park, C.-M. Electrochemical characteristics of ZnSe and its nanostructured composite for rechargeable Li-ion batteries. *J. Power Sources* **2014**, *251*, 319–324. [[CrossRef](#)]
22. Wang, J.; Chen, L.; Zeng, L.; Wei, Q.; Wei, M. In Situ Synthesis of WSe₂/CMK-5 Nanocomposite for Rechargeable Lithium-Ion Batteries with a Long-Term Cycling Stability. *ACS Sustain. Chem. Eng.* **2018**, *6*, 4688–4694. [[CrossRef](#)]
23. Zhao, X.; Wang, H.-E.; Yang, Y.; Neale, Z.G.; Massé, R.C.; Cao, J.; Cai, W.; Sui, J.; Cao, G. Reversible and fast Na-ion storage in MoO₂/MoSe₂ heterostructures for high energy-high power Na-ion capacitors. *Energy Storage Mater.* **2018**, *12*, 241–251. [[CrossRef](#)]
24. Ersan, F.; Gökoğlu, G.; Aktürk, E. Adsorption and Diffusion of Lithium on Monolayer Transition Metal Dichalcogenides (MoS₂(1-x)Se₂x) Alloys. *J. Phys. Chem. C* **2015**, *119*, 28648–28653. [[CrossRef](#)]
25. Yang, E.; Ji, H.; Jung, Y. Two-Dimensional Transition Metal Dichalcogenide Monolayers as Promising Sodium Ion Battery Anodes. *J. Phys. Chem. C* **2015**, *119*, 26374–26380. [[CrossRef](#)]
26. Xiao, Y.; Lee, S.H.; Sun, Y.-K. The Application of Metal Sulfides in Sodium Ion Batteries. *Adv. Energy Mater.* **2017**, *7*, 1601329. [[CrossRef](#)]
27. Yang, K.; Zhang, X.; Song, K.; Zhang, J.; Liu, C.; Mi, L.; Wang, Y.; Chen, W. Se–C bond and reversible SEI in facile synthesized SnSe₂/3D carbon induced stable anode for sodium-ion batteries. *Electrochim. Acta* **2020**, *337*, 135783. [[CrossRef](#)]
28. Yu, S.-H.; Zachman, M.J.; Kang, K.; Gao, H.; Huang, X.; DiSalvo, F.J.; Park, J.; Kourkoutis, L.F.; Abruña, H.D. Atomic-Scale Visualization of Electrochemical Lithiation Processes in Monolayer MoS₂ by Cryogenic Electron Microscopy. *Adv. Energy Mater.* **2019**, *9*, 1902773. [[CrossRef](#)]
29. Wang, K.; Hua, W.; Li, Z.; Wang, Q.; Kubel, C.; Mu, X. New Insight into Desodiation/Sodiation Mechanism of MoS₂: Sodium Insertion in Amorphous Mo-S Clusters. *ACS Appl. Mater. Interfaces* **2021**, *13*, 40481–40488. [[CrossRef](#)]
30. Xie, D.; Tang, W.; Wang, Y.; Xia, X.; Zhong, Y.; Zhou, D.; Wang, D.; Wang, X.; Tu, J. Facile fabrication of integrated three-dimensional C-MoSe₂/reduced graphene oxide composite with enhanced performance for sodium storage. *Nano Res.* **2016**, *9*, 1618–1629. [[CrossRef](#)]
31. Plewa, A.; Kulka, A.; Hanc, E.; Sun, J.; Nowak, M.; Redel, K.; Lu, L.; Molenda, J. Abnormal Phenomena of Multi-Way Sodium Storage in Selenide Electrode. *Adv. Funct. Mater.* **2021**, *31*, 2102406. [[CrossRef](#)]
32. Yuan, D.; Dou, Y.; Tian, Y.; Adekoya, D.; Xu, L.; Zhang, S. Robust Pseudocapacitive Sodium Cation Intercalation Induced by Cobalt Vacancies at Atomically Thin Co_(1-x)Se₂/Graphene Heterostructure for Sodium-Ion Batteries. *Angew. Chem. Int. Ed. Engl.* **2021**, *60*, 18830–18837. [[CrossRef](#)] [[PubMed](#)]
33. Lin, X.M.; Chen, J.H.; Fan, J.J.; Ma, Y.; Radjenovic, P.; Xu, Q.C.; Huang, L.; Passerini, S.; Tian, Z.Q.; Li, J.F. Synthesis and Operando Sodiation Mechanistic Study of Nitrogen-Doped Porous Carbon Coated Bimetallic Sulfide Hollow Nanocubes as Advanced Sodium Ion Battery Anode. *Adv. Energy Mater.* **2019**, *9*, 1902312. [[CrossRef](#)]
34. Cao, L.; Zhang, B.; Ou, X.; Wang, C.; Peng, C.; Zhang, J. Synergistical Coupling Interconnected ZnS/SnS₂ Nanoboxes with Polypyrrole-Derived N/S Dual-Doped Carbon for Boosting High-Performance Sodium Storage. *Small* **2019**, *15*, 1804861. [[CrossRef](#)]
35. Wang, Y.-X.; Yang, J.; Chou, S.-L.; Liu, H.K.; Zhang, W.-X.; Zhao, D.; Dou, S.X. Uniform yolk-shell iron sulfide–carbon nanospheres for superior sodium–iron sulfide batteries. *Nat. Commun.* **2015**, *6*, 8689. [[CrossRef](#)] [[PubMed](#)]
36. Nasrollahpour, M.; Vafaei, M.; Hosseini, M.R.; Iravani, H. Ab initio study of sodium diffusion and adsorption on boron-doped graphyne as promising anode material in sodium-ion batteries. *Phys. Chem. Chem. Phys.* **2018**, *20*, 29889–29895. [[CrossRef](#)] [[PubMed](#)]
37. Tabassum, H.; Zou, R.; Mahmood, A.; Liang, Z.; Wang, Q.; Zhang, H.; Gao, S.; Qu, C.; Guo, W.; Guo, S. A Universal Strategy for Hollow Metal Oxide Nanoparticles Encapsulated into B/N Co-Doped Graphitic Nanotubes as High-Performance Lithium-Ion Battery Anodes. *Adv. Mater.* **2018**, *30*, 1705441. [[CrossRef](#)] [[PubMed](#)]

38. Pomerantseva, E.; Bonaccorso, F.; Feng, X.; Cui, Y.; Gogotsi, Y. Energy storage: The future enabled by nanomaterials. *Science* **2019**, *366*, eaan8285. [[CrossRef](#)]
39. Guo, Q.; Ma, Y.; Chen, T.; Xia, Q.; Yang, M.; Xia, H.; Yu, Y. Cobalt Sulfide Quantum Dot Embedded N/S-Doped Carbon Nanosheets with Superior Reversibility and Rate Capability for Sodium-Ion Batteries. *ACS Nano* **2017**, *11*, 12658–12667. [[CrossRef](#)]
40. Wang, C.; Zhang, Y.; Li, Y.; Zhang, Y.; Dong, Y.; Li, D.; Zhang, J. Construction of uniform SnS₂/ZnS heterostructure nanosheets embedded in graphene for advanced lithium-ion batteries. *J. Alloys Compd.* **2020**, *820*, 153147. [[CrossRef](#)]
41. Xiao, Y.; Sun, P.F.; Cao, M. Core-shell bimetallic carbide nanoparticles confined in a three-dimensional N-doped carbon conductive network for efficient lithium storage. *ACS Nano* **2014**, *8*, 7846–7857. [[CrossRef](#)]
42. Lei, C.; Han, F.; Li, D.; Li, W.-C.; Sun, Q.; Zhang, X.-Q.; Lu, A.-H. Dopamine as the coating agent and carbon precursor for the fabrication of N-doped carbon coated Fe₃O₄ composites as superior lithium ion anodes. *Nanoscale* **2013**, *5*, 1168–1175. [[CrossRef](#)] [[PubMed](#)]
43. Peng, C.; Chen, B.; Qin, Y.; Yang, S.; Li, C.; Zuo, Y.; Liu, S.; Yang, J. Facile Ultrasonic Synthesis of CoO Quantum Dot/Graphene Nanosheet Composites with High Lithium Storage Capacity. *ACS Nano* **2012**, *6*, 1074–1081. [[CrossRef](#)] [[PubMed](#)]
44. Firmiano, E.G.S.; Cordeiro, M.A.L.; Rabelo, A.C.; Dalmaschio, C.J.; Pinheiro, A.N.; Pereira, E.C.; Leite, E.R. Graphene oxide as a highly selective substrate to synthesize a layered MoS₂ hybrid electrocatalyst. *Chem. Commun.* **2012**, *48*, 7687–7689. [[CrossRef](#)] [[PubMed](#)]
45. Zhang, X.-F.; Ma, X.; Hou, T.; Guo, K.; Yin, J.; Wang, Z.; Shu, L.; He, M.; Yao, J. Inorganic Salts Induce Thermally Reversible and Anti-Freezing Cellulose Hydrogels. *Angew. Chem. Int. Ed.* **2019**, *58*, 7366–7370. [[CrossRef](#)] [[PubMed](#)]
46. Chen, Z.; Wu, R.; Liu, M.; Wang, H.; Xu, H.; Guo, Y.; Song, Y.; Fang, F.; Yu, X.; Sun, D. General Synthesis of Dual Carbon-Confined Metal Sulfides Quantum Dots Toward High-Performance Anodes for Sodium-Ion Batteries. *Adv. Funct. Mater.* **2017**, *27*, 1702046. [[CrossRef](#)]
47. Xia, G.; Zhang, L.; Fang, F.; Sun, D.; Guo, Z.; Liu, H.; Yu, X. General Synthesis of Transition Metal Oxide Ultrafine Nanoparticles Embedded in Hierarchically Porous Carbon Nanofibers as Advanced Electrodes for Lithium Storage. *Adv. Funct. Mater.* **2016**, *26*, 6188–6196. [[CrossRef](#)]
48. Yuan, Z.; Dong, L.; Gao, Q.; Huang, Z.; Wang, L.; Wang, G.; Yu, X. SnSb alloy nanoparticles embedded in N-doped porous carbon nanofibers as a high-capacity anode material for lithium-ion batteries. *J. Alloys Compd.* **2019**, *777*, 775–783. [[CrossRef](#)]
49. Cheng, Q.; Li, Y.; Gao, P.; Xia, G.; He, S.; Yang, Y.; Pan, H.; Yu, X. Lithium Azides Induced SnS Quantum Dots for Ultra-Fast and Long-Term Sodium Storage. *Small* **2023**, *19*, 2302188. [[CrossRef](#)]
50. Jin, T.; Han, Q.; Wang, Y.; Jiao, L. 1D Nanomaterials: Design, Synthesis, and Applications in Sodium-Ion Batteries. *Small* **2018**, *14*, 1703086. [[CrossRef](#)]
51. Chen, Z.; Chen, G.; Wang, C.; Chen, D.; Zhang, Q.; Jiang, L.; Zhang, C.; Liu, K.; He, S. Capacitive properties of carbon nanofibers derived from blends of cellulose acetate and polyacrylonitrile. *New J. Chem.* **2023**, *47*, 13831–13840. [[CrossRef](#)]
52. Xu, X.; Li, F.; Zhang, D.; Liu, Z.; Zuo, S.; Zeng, Z.; Liu, J. Self-Sacrifice Template Construction of Uniform Yolk-Shell ZnS@C for Superior Alkali-Ion Storage. *Adv. Sci.* **2022**, *9*, e2200247. [[CrossRef](#)] [[PubMed](#)]
53. Yang, X.; Zhang, J.; Wang, Z.; Wang, H.; Zhi, C.; Yu, D.Y.W.; Rogach, A.L. Carbon-Supported Nickel Selenide Hollow Nanowires as Advanced Anode Materials for Sodium-Ion Batteries. *Small* **2018**, *14*, 1702669. [[CrossRef](#)] [[PubMed](#)]
54. Wei, P.; Zhu, J.; Qiu, Y.; Wang, G.; Xu, X.; Ma, S.; Shen, P.K.; Wu, X.L.; Yamauchi, Y. One-dimensional core-shell motif nanowires with chemically-bonded transition metal sulfide-carbon heterostructures for efficient sodium-ion storage. *Chem. Sci.* **2021**, *12*, 15054–15060. [[CrossRef](#)] [[PubMed](#)]
55. Hong, Y.J.; Kim, J.H.; Chan Kang, Y. Sodium-ion storage performance of hierarchically structured (Co_{1/3}Fe_{2/3})Se₂ nanofibers with fiber-in-tube nanostructures. *J. Mater. Chem. A* **2016**, *4*, 15471–15477. [[CrossRef](#)]
56. Zhang, Y.; Chen, Y.; Jiang, Y.; Wang, J.; Zheng, X.; Han, B.; Xia, K.; Gao, Q.; Cai, Z.; Zhou, C.; et al. Construction of VS₂/VO_x Heterostructure via Hydrolysis-Oxidation Coupling Reaction with Superior Sodium Storage Properties. *Adv. Funct. Mater.* **2023**, *33*, 2212785. [[CrossRef](#)]
57. Wen, X.; Feng, W.; Li, X.; Yang, J.; Du, R.; Wang, P.; Li, H.; Song, L.; Wang, Y.; Cheng, M.; et al. Diatomite-Templated Synthesis of Single-Atom Cobalt-Doped MoS₂/Carbon Composites to Boost Sodium Storage. *Adv. Mater.* **2023**, *35*, e2211690. [[CrossRef](#)]
58. Yuan, Z.; Wang, L.; Li, D.; Cao, J.; Han, W. Carbon-Reinforced Nb₂CT_x MXene/MoS₂ Nanosheets as a Superior Rate and High-Capacity Anode for Sodium-Ion Batteries. *ACS Nano* **2021**, *15*, 7439–7450. [[CrossRef](#)]
59. Liu, T.; Ding, J.; Su, Z.; Wei, G. Porous two-dimensional materials for energy applications: Innovations and challenges. *Mater. Today Energy* **2017**, *6*, 79–95. [[CrossRef](#)]
60. Zhang, Q.; Yan, B.; Feng, L.; Zheng, J.; You, B.; Chen, J.; Zhao, X.; Zhang, C.; Jiang, S.; He, S. Progress in the use of organic potassium salts for the synthesis of porous carbon nanomaterials: Microstructure engineering for advanced supercapacitors. *Nanoscale* **2022**, *14*, 8216–8244. [[CrossRef](#)]
61. Li, X.; Han, Z.; Yang, W.; Li, Q.; Li, H.; Xu, J.; Li, H.; Liu, B.; Zhao, H.; Li, S.; et al. 3D Ordered Porous Hybrid of ZnSe/N-doped Carbon with Anomalously High Na⁺ Mobility and Ultrathin Solid Electrolyte Interphase for Sodium-Ion Batteries. *Adv. Funct. Mater.* **2021**, *31*, 2106194. [[CrossRef](#)]
62. Ge, P.; Li, S.; Xu, L.; Zou, K.; Gao, X.; Cao, X.; Zou, G.; Hou, H.; Ji, X. Hierarchical Hollow-Microsphere Metal-Selenide@Carbon Composites with Rational Surface Engineering for Advanced Sodium Storage. *Adv. Energy Mater.* **2019**, *9*, 1803035. [[CrossRef](#)]
63. Park, G.D.; Kang, Y.C. Multiroom-structured multicomponent metal selenide-graphitic carbon-carbon nanotube hybrid microspheres as efficient anode materials for sodium-ion batteries. *Nanoscale* **2018**, *10*, 8125–8132. [[CrossRef](#)] [[PubMed](#)]

64. Xiao, Q.; Song, Q.; Zheng, K.; Zheng, L.; Zhu, Y.; Chen, Z. CoSe₂ nanodots confined in multidimensional porous nanoarchitecture towards efficient sodium ion storage. *Nano Energy* **2022**, *98*, 107326. [[CrossRef](#)]
65. Shang, Y.; Li, X.; Huang, S.; Chen, S.; Yang, Z.; Guo, L.; Yang, H.Y. A Selective Reduction Approach to Construct Robust Cu_{1.81}S Truss Structures for High-Performance Sodium Storage. *Matter* **2020**, *2*, 428–439. [[CrossRef](#)]
66. Jiang, H.; Huang, L.; Wei, Y.; Wang, B.; Wu, H.; Zhang, Y.; Liu, H.; Dou, S. Bio-Derived Hierarchical Multicore–Shell Fe₂N-Nanoparticle-Impregnated N-Doped Carbon Nanofiber Bundles: A Host Material for Lithium-/Potassium-Ion Storage. *Nano-Micro Lett.* **2019**, *11*, 56. [[CrossRef](#)]
67. Mai, L.; Sheng, J.; Xu, L.; Tan, S.; Meng, J. One-Dimensional Hetero-Nanostructures for Rechargeable Batteries. *Acc. Chem. Res.* **2018**, *51*, 950–959. [[CrossRef](#)]
68. Hasa, I.; Hassoun, J.; Passerini, S. Nanostructured Na-ion and Li-ion anodes for battery application: A comparative overview. *Nano Res.* **2017**, *10*, 3942–3969. [[CrossRef](#)]
69. Wu, Y.; Yu, Y. 2D material as anode for sodium ion batteries: Recent progress and perspectives. *Energy Storage Mater.* **2019**, *16*, 323–343. [[CrossRef](#)]
70. Lu, Y.; Yu, L.; Lou, X.W. Nanostructured Conversion-type Anode Materials for Advanced Lithium-Ion Batteries. *Chem* **2018**, *4*, 972–996. [[CrossRef](#)]
71. Li, N.-W.; Yin, Y.-X.; Xin, S.; Li, J.-Y.; Guo, Y.-G. Methods for the Stabilization of Nanostructured Electrode Materials for Advanced Rechargeable Batteries. *Small Methods* **2017**, *1*, 1700094. [[CrossRef](#)]
72. Wang, Y.; Wang, Z.; Chen, Y.; Zhang, H.; Yousaf, M.; Wu, H.; Zou, M.; Cao, A.; Han, R.P.S. Hyperporous Sponge Interconnected by Hierarchical Carbon Nanotubes as a High-Performance Potassium-Ion Battery Anode. *Adv. Mater.* **2018**, *30*, 1802074. [[CrossRef](#)] [[PubMed](#)]
73. Zhou, L.; Cao, Z.; Zhang, J.; Cheng, H.; Liu, G.; Park, G.T.; Cavallo, L.; Wang, L.; Alshareef, H.N.; Sun, Y.K.; et al. Electrolyte-Mediated Stabilization of High-Capacity Micro-Sized Antimony Anodes for Potassium-Ion Batteries. *Adv. Mater.* **2021**, *33*, e2005993. [[CrossRef](#)] [[PubMed](#)]
74. Zhang, Y.; Tao, L.; Xie, C.; Wang, D.; Zou, Y.; Chen, R.; Wang, Y.; Jia, C.; Wang, S. Defect Engineering on Electrode Materials for Rechargeable Batteries. *Adv. Mater.* **2020**, *32*, 1905923. [[CrossRef](#)] [[PubMed](#)]
75. Huang, Y.; Wang, M.; Huang, M.; Xiong, Y.; Yang, X.; Miao, Z.; Yang, Z.; Yu, J. Co_{0.85}Se@carbon nanotubes surface-seeding grown on carbon microplates as superior anode material for sodium ion batteries. *Electrochim. Acta* **2022**, *414*, 140167. [[CrossRef](#)]
76. Zhou, H.; Li, Z.; Wang, K.; Gao, M.; Ding, S. Phase boundary-enhanced Ni₃N–Co₃N@CNT composite materials for lithium-ion batteries. *J. Mater. Chem. A* **2019**, *7*, 1779–1784. [[CrossRef](#)]
77. Wang, S.; Yang, Y.; Quan, W.; Hong, Y.; Zhang, Z.; Tang, Z.; Li, J. Ti³⁺-free three-phase Li₄Ti₅O₁₂/TiO₂ for high-rate lithium ion batteries: Capacity and conductivity enhancement by phase boundaries. *Nano Energy* **2017**, *32*, 294–301. [[CrossRef](#)]
78. Zhang, D.M.; Jia, J.H.; Yang, C.C.; Jiang, Q. Fe₇Se₈ nanoparticles anchored on N-doped carbon nanofibers as high-rate anode for sodium-ion batteries. *Energy Storage Mater.* **2020**, *24*, 439–449. [[CrossRef](#)]
79. Li, Y.; Qian, J.; Zhang, M.; Wang, S.; Wang, Z.; Li, M.; Bai, Y.; An, Q.; Xu, H.; Wu, F.; et al. Co-Construction of Sulfur Vacancies and Heterojunctions in Tungsten Disulfide to Induce Fast Electronic/Ionic Diffusion Kinetics for Sodium-Ion Batteries. *Adv. Mater.* **2020**, *32*, e2005802. [[CrossRef](#)]
80. Su, Q.; Cao, X.; Yu, T.; Kong, X.; Wang, Y.; Chen, J.; Lin, J.; Xie, X.; Liang, S.; Pan, A. Binding MoSe₂ with dual protection carbon for high-performance sodium storage. *J. Mater. Chem. A* **2019**, *7*, 22871–22878. [[CrossRef](#)]
81. Zhao, X.; Gong, F.; Zhao, Y.; Huang, B.; Qian, D.; Wang, H.-E.; Zhang, W.; Yang, Z. Encapsulating NiS nanocrystal into nitrogen-doped carbon framework for high performance sodium/potassium-ion storage. *Chem. Eng. J.* **2020**, *392*, 123675. [[CrossRef](#)]
82. Hou, J.; Zhu, Z.; Li, C.; Zhang, J.; Shen, S.; Yao, Z.; Liu, T.; Li, W.; Xia, X.; Yang, Y. Spatially Confined Synthesis of SnSe Spheres Encapsulated in N, Se Dual-Doped Carbon Networks toward Fast and Durable Sodium Storage. *ACS Appl. Mater. Interfaces* **2022**, *14*, 4230–4241. [[CrossRef](#)] [[PubMed](#)]
83. Liu, P.; Han, J.; Zhu, K.; Dong, Z.; Jiao, L. Heterostructure SnSe₂/ZnSe@PDA Nanobox for Stable and Highly Efficient Sodium-Ion Storage. *Adv. Energy Mater.* **2020**, *10*, 2000741. [[CrossRef](#)]
84. Yu, H.; Jiang, G.; Ni, J.; Li, L. Architecting core-shell nanosheets of MoS₂-polypyrrole on carbon cloth as a robust sodium anode. *Sustain. Mater. Technol.* **2021**, *28*, e00255. [[CrossRef](#)]
85. Zang, R.; Li, P.; Guo, X.; Man, Z.; Zhang, S.; Wang, C.; Wang, G. Yolk-shell N-doped carbon coated FeS₂ nanocages as a high-performance anode for sodium-ion batteries. *J. Mater. Chem. A* **2019**, *7*, 14051–14059. [[CrossRef](#)]
86. Li, X.; Yang, X.; Xue, H.; Pang, H.; Xu, Q. Metal-organic frameworks as a platform for clean energy applications. *EnergyChem* **2020**, *2*, 100027. [[CrossRef](#)]
87. Zhao, Y.; Fu, Q.; Wang, D.; Pang, Q.; Gao, Y.; Missiul, A.; Nemausat, R.; Sarapulova, A.; Ehrenberg, H.; Wei, Y.; et al. Co₉S₈@carbon yolk-shell nanocages as a high performance direct conversion anode material for sodium ion batteries. *Energy Storage Mater.* **2019**, *18*, 51–58. [[CrossRef](#)]
88. Zhou, P.; Zhang, M.; Wang, L.; Huang, Q.; Su, Z.; Xu, P.; Zou, R.; Wang, X.; Zeng, C.; Ba, K. MOFs-Derived Flower-Like Hierarchically Porous Zn-Mn-Se/C Composite for Extraordinary Rate Performance and Durable Anode of Sodium-Ion and Potassium-Ion Batteries. *Small* **2022**, *18*, e2203964. [[CrossRef](#)]

89. Yousaf, M.; Wang, Z.; Wang, Y.; Chen, Y.; Ali, U.; Maqbool, M.; Imran, A.; Mahmood, N.; Gao, P.; Han, R.P.S. Core-Shell FeSe₂/C Nanostructures Embedded in a Carbon Framework as a Free Standing Anode for a Sodium Ion Battery. *Small* **2020**, *16*, e2002200. [[CrossRef](#)]
90. Kong, Z.; Huang, M.; Liang, Z.; Tu, H.; Zhang, K.; Shao, Y.; Wu, Y.; Hao, X. Phosphorus doping induced the co-construction of sulfur vacancies and heterojunctions in tin disulfide as a durable anode for lithium/sodium-ion batteries. *Inorg. Chem. Front.* **2022**, *9*, 902–913. [[CrossRef](#)]
91. Kiciński, W.; Szala, M.; Bystrzejewski, M. Sulfur-doped porous carbons: Synthesis and applications. *Carbon* **2014**, *68*, 1–32. [[CrossRef](#)]
92. Jiang, Y.; Xie, M.; Wu, F.; Ye, Z.; Zhang, Y.; Wang, Z.; Zhou, Y.; Li, L.; Chen, R. Cobalt Selenide Hollow Polyhedron Encapsulated in Graphene for High-Performance Lithium/Sodium Storage. *Small* **2021**, *17*, e2102893. [[CrossRef](#)] [[PubMed](#)]
93. Yang, C.; Liang, X.; Ou, X.; Zhang, Q.; Zheng, H.S.; Zheng, F.; Wang, J.H.; Huang, K.; Liu, M. Heterostructured Nanocube-Shaped Binary Sulfide (SnCo)S₂ Interlaced with S-Doped Graphene as a High-Performance Anode for Advanced Na⁺ Batteries. *Adv. Funct. Mater.* **2019**, *29*, 1807971. [[CrossRef](#)]
94. Ye, J.; Li, X.; Xia, G.; Gong, G.; Zheng, Z.; Chen, C.; Hu, C. P-doped CoSe₂ nanoparticles embedded in 3D honeycomb-like carbon network for long cycle-life Na-ion batteries. *J. Mater. Sci. Technol.* **2021**, *77*, 100–107. [[CrossRef](#)]
95. Zhang, H.; Wang, T.; Sumboja, A.; Zang, W.; Xie, J.; Gao, D.; Pennycook, S.J.; Liu, Z.; Guan, C.; Wang, J. Integrated Hierarchical Carbon Flake Arrays with Hollow P-Doped CoSe₂ Nanoclusters as an Advanced Bifunctional Catalyst for Zn–Air Batteries. *Adv. Funct. Mater.* **2018**, *28*, 1804846. [[CrossRef](#)]
96. Wang, L.; Han, Z.; Zhao, Q.; Yao, X.; Zhu, Y.; Ma, X.; Wu, S.; Cao, C. Engineering yolk–shell P-doped NiS₂/C spheres via a MOF-template for high-performance sodium-ion batteries. *J. Mater. Chem. A* **2020**, *8*, 8612–8619. [[CrossRef](#)]
97. Ma, X.; Li, Y.; Long, X.; Luo, H.-C.; Xu, C.; Wang, G.; Zhao, W. Construction of phosphorus-doping with spontaneously developed selenium vacancies: Inducing superior ion-diffusion kinetics in hollow Cu₂Se@C nanospheres for efficient sodium storage. *J. Energy Chem.* **2022**, *77*, 227–238. [[CrossRef](#)]
98. Niu, F.; Yang, J.; Wang, N.; Zhang, D.; Fan, W.; Yang, J.; Qian, Y. MoSe₂-Covered N,P-Doped Carbon Nanosheets as a Long-Life and High-Rate Anode Material for Sodium-Ion Batteries. *Adv. Funct. Mater.* **2017**, *27*, 1700522. [[CrossRef](#)]
99. Xu, L.; Guo, W.; Zeng, L.; Xia, X.; Wang, Y.; Xiong, P.; Chen, Q.; Zhang, J.; Wei, M.; Qian, Q. V₃Se₄ embedded within N/P co-doped carbon fibers for sodium/potassium ion batteries. *Chem. Eng. J.* **2021**, *419*, 129607. [[CrossRef](#)]
100. Ma, X.; Diao, L.; Wang, Y.; Zhang, L.; Lu, Y.; Li, D.; Yang, D.; She, X. S-vacancies manipulating enhances Na⁺ insertion of MoS₂ for efficient sodium-ion storage. *Chem. Eng. J.* **2023**, *457*, 141116. [[CrossRef](#)]
101. Zhao, C.; Li, Y.; Zhang, W.; Zheng, Y.; Lou, X.; Yu, B.; Chen, J.; Chen, Y.; Liu, M.; Wang, J. Heterointerface engineering for enhancing the electrochemical performance of solid oxide cells. *Energy Environ. Sci.* **2020**, *13*, 53–85. [[CrossRef](#)]
102. Zhang, Y.; Wang, N.; Sun, C.; Lu, Z.; Xue, P.; Tang, B.; Bai, Z.; Dou, S. 3D spongy CoS₂ nanoparticles/carbon composite as high-performance anode material for lithium/sodium ion batteries. *Chem. Eng. J.* **2018**, *332*, 370–376. [[CrossRef](#)]
103. Lian, Y.; Chen, F.; Kang, H.; Wu, C.; Zhang, M.; Xu, S. Co₉S₈ nanoparticles scaffolded within carbon-nanoparticles-decorated carbon spheres as anodes for lithium and sodium storage. *Appl. Surf. Sci.* **2020**, *507*, 145061. [[CrossRef](#)]
104. Shuang, W.; Huang, H.; Kong, L.; Zhong, M.; Li, A.; Wang, D.; Xu, Y.; Bu, X.-H. Nitrogen-doped carbon shell-confined Ni₃S₂ composite nanosheets derived from Ni-MOF for high performance sodium-ion battery anodes. *Nano Energy* **2019**, *62*, 154–163. [[CrossRef](#)]
105. Naguib, M.; Kurtoglu, M.; Presser, V.; Lu, J.; Niu, J.; Heon, M.; Hultman, L.; Gogotsi, Y.; Barsoum, M.W. Two-Dimensional Nanocrystals Produced by Exfoliation of Ti₃AlC₂. *Adv. Mater.* **2011**, *23*, 4248–4253. [[CrossRef](#)] [[PubMed](#)]
106. Li, J.; Li, Z.; Liu, X.; Li, C.; Zheng, Y.; Yeung, K.W.K.; Cui, Z.; Liang, Y.; Zhu, S.; Hu, W.; et al. Interfacial engineering of Bi₂S₃/Ti₃C₂T_x MXene based on work function for rapid photo-excited bacteria-killing. *Nat. Commun.* **2021**, *12*, 1224. [[CrossRef](#)] [[PubMed](#)]
107. Huang, P.; Ying, H.; Zhang, S.; Zhang, Z.; Han, W.Q. Molten Salts Etching Route Driven Universal Construction of MXene/Transition Metal Sulfides Heterostructures with Interfacial Electronic Coupling for Superior Sodium Storage. *Adv. Energy Mater.* **2022**, *12*, 2202052. [[CrossRef](#)]
108. Sun, Z.; Liang, H.; Wang, H.; Shi, J.; Huang, M.; Chen, J.; Liu, S.; Tian, W.; Cao, H.; Li, Z. Spatially Confined “Edge-to-Edge” Strategy for Achieving Compact Na⁺/K⁺ Storage: Constructing Hetero-Ni/Ni₃S₂ in Densified Carbons. *Adv. Funct. Mater.* **2022**, *32*, 2203291. [[CrossRef](#)]
109. Guo, C.; Zhang, W.; Liu, Y.; He, J.; Yang, S.; Liu, M.; Wang, Q.; Guo, Z. Constructing CoO/Co₃S₄ Heterostructures Embedded in N-doped Carbon Frameworks for High-Performance Sodium-Ion Batteries. *Adv. Funct. Mater.* **2019**, *29*, 1901925. [[CrossRef](#)]
110. Zhang, C.; Han, F.; Wang, F.; Liu, Q.; Zhou, D.; Zhang, F.; Xu, S.; Fan, C.; Li, X.; Liu, J. Improving compactness and reaction kinetics of MoS₂@C anodes by introducing Fe₉S₁₀ core for superior volumetric sodium/potassium storage. *Energy Storage Mater.* **2020**, *24*, 208–219. [[CrossRef](#)]
111. Cao, L.; Liang, X.; Ou, X.; Yang, X.; Li, Y.; Yang, C.; Lin, Z.; Liu, M. Heterointerface Engineering of Hierarchical Bi₂S₃/MoS₂ with Self-Generated Rich Phase Boundaries for Superior Sodium Storage Performance. *Adv. Funct. Mater.* **2020**, *30*, 1910732. [[CrossRef](#)]
112. Li, H. Interface engineering renders high-rate high-capacity lithium storage in black phosphorous composite anodes with excellent cycling durability. *Sci. China Chem.* **2020**, *63*, 1734–1736. [[CrossRef](#)]

113. Chen, W.; Qi, S.; Guan, L.; Liu, C.; Cui, S.; Shen, C.; Mi, L. Pyrite FeS₂ microspheres anchoring on reduced graphene oxide aerogel as an enhanced electrode material for sodium-ion batteries. *J. Mater. Chem. A* **2017**, *5*, 5332–5341. [[CrossRef](#)]
114. Wang, J.; Yin, H.; Wang, Z.; Gao, J.; Jiang, Q.; Xu, Y.; Chen, Z. High-performance Sn-based anode with robust lignin-derived hard carbon support for sodium-ion batteries. *Asia-Pac. J. Chem. Eng.* **2022**, *17*, e2768. [[CrossRef](#)]
115. Yang, L.; Liu, M.; Xiang, Y.; Deng, W.; Zou, G.; Hou, H.; Ji, X. Carbon skeleton confined Sb chalcogenides nanodots for stable sodium storage. *Carbon* **2022**, *197*, 341–349. [[CrossRef](#)]
116. Wang, M.; Yang, Y.; Yang, Z.; Gu, L.; Chen, Q.; Yu, Y. Sodium-Ion Batteries: Improving the Rate Capability of 3D Interconnected Carbon Nanofibers Thin Film by Boron, Nitrogen Dual-Doping. *Adv. Sci.* **2017**, *4*, 1600468. [[CrossRef](#)]
117. Liu, S.; Ren, Z.; Fakudze, S.; Shang, Q.; Chen, J.; Liu, C.; Han, J.; Tian, Z. Structural Evolution of Graphitic Carbon Derived from Ionic Liquids-Dissolved Cellulose and Its Application as Lithium-Ion Battery Anodes. *Langmuir* **2022**, *38*, 320–331. [[CrossRef](#)]
118. Sun, Q.; Li, D.; Dai, L.; Liang, Z.; Ci, L. Structural Engineering of SnS₂ Encapsulated in Carbon Nanoboxes for High-Performance Sodium/Potassium-Ion Batteries Anodes. *Small* **2020**, *16*, e2005023. [[CrossRef](#)]
119. Jayaramulu, K.; Mukherjee, S.; Morales, D.M.; Dubal, D.P.; Nanjundan, A.K.; Schneemann, A.; Masa, J.; Kment, S.; Schuhmann, W.; Otyepka, M.; et al. Graphene-Based Metal–Organic Framework Hybrids for Applications in Catalysis, Environmental, and Energy Technologies. *Chem. Rev.* **2022**, *122*, 17241–17338. [[CrossRef](#)]
120. Ding, Y.-L.; Kopold, P.; Hahn, K.; van Aken, P.A.; Maier, J.; Yu, Y. A Lamellar Hybrid Assembled from Metal Disulfide Nanowall Arrays Anchored on a Carbon Layer: In Situ Hybridization and Improved Sodium Storage. *Adv. Mater.* **2016**, *28*, 7774–7782. [[CrossRef](#)]
121. Quan, Y.; Chen, M.; Zhou, W.; Tian, Q.; Chen, J. High-Performance Anti-freezing Flexible Zn-MnO₂ Battery Based on Polyacrylamide/Graphene Oxide/Ethylene Glycol Gel Electrolyte. *Front. Chem.* **2020**, *8*, 603. [[CrossRef](#)]
122. Zhao, X.; He, D.; You, B. Laser engraving and punching of graphene films as flexible all-solid-state planar micro-supercapacitor electrodes. *Mater. Today Sustain.* **2022**, *17*, 100096. [[CrossRef](#)]
123. Zhao, X.; Cai, W.; Yang, Y.; Song, X.; Neale, Z.; Wang, H.-E.; Sui, J.; Cao, G. MoSe₂ nanosheets perpendicularly grown on graphene with Mo–C bonding for sodium-ion capacitors. *Nano Energy* **2018**, *47*, 224–234. [[CrossRef](#)]
124. Li, H.; Ma, Y.; Zhang, H.; Diemant, T.; Behm, R.J.; Varzi, A.; Passerini, S. Metal–Organic Framework Derived Fe₇S₈ Nanoparticles Embedded in Heteroatom-Doped Carbon with Lithium and Sodium Storage Capability. *Small Methods* **2020**, *4*, 2000637. [[CrossRef](#)]
125. Zhao, W.; Gao, L.; Ma, X.; Yue, L.; Zhao, D.; Li, Z.; Sun, S.; Luo, Y.; Liu, Q.; Asiri, A.M.; et al. An exquisite branch–leaf shaped metal sulfoselenide composite endowing an ultrastable sodium-storage lifespan over 10,000 cycles. *J. Mater. Chem. A* **2022**, *10*, 16962–16975. [[CrossRef](#)]
126. Lipatov, A.; Alhabeab, M.; Lukatskaya, M.R.; Boson, A.; Gogotsi, Y.; Sinitskii, A. Effect of Synthesis on Quality, Electronic Properties and Environmental Stability of Individual Monolayer Ti₃C₂ MXene Flakes. *Adv. Electron. Mater.* **2016**, *2*, 1600255.
127. Zhang, J.; Zhao, Y.; Guo, X.; Chen, C.; Dong, C.-L.; Liu, R.-S.; Han, C.-P.; Li, Y.; Gogotsi, Y.; Wang, G. Single platinum atoms immobilized on an MXene as an efficient catalyst for the hydrogen evolution reaction. *Nat. Catal.* **2018**, *1*, 985–992. [[CrossRef](#)]
128. Li, Q.; Jiao, Q.; Yan, Y.; Li, H.; Zhou, W.; Gu, T.; Shen, X.; Lu, C.; Zhao, Y.; Zhang, Y.; et al. Optimized Co–S bonds energy and confinement effect of hollow MXene@CoS₂/NC for enhanced sodium storage kinetics and stability. *Chem. Eng. J.* **2022**, *450*, 137922. [[CrossRef](#)]
129. Chen, S.; Huang, S.; Zhang, Y.-F.; Fan, S.; Yan, D.; Shang, Y.; Pam, M.E.; Ge, Q.; Shi, Y.; Yang, H.Y. Constructing stress-release layer on Fe₇Se₈-based composite for highly stable sodium-storage. *Nano Energy* **2020**, *69*, 104389. [[CrossRef](#)]
130. Dong, C.; Wu, L.; He, Y.; Zhou, Y.; Sun, X.; Du, W.; Sun, X.; Xu, L.; Jiang, F. Willow-Leaf-Like ZnSe@N-Doped Carbon Nanoarchitecture as a Stable and High-Performance Anode Material for Sodium-Ion and Potassium-Ion Batteries. *Small* **2020**, *16*, e2004580. [[CrossRef](#)]
131. Dong, S.; Su, Q.; Jiao, W.; Ding, S.; Zhang, M.; Du, G.; Xu, B. FeSe₂ microspheres coated with carbon layers as anode materials for sodium-ion batteries. *J. Alloys Compd.* **2020**, *842*, 155888. [[CrossRef](#)]
132. Jiang, S.; Xiang, M.; Zhang, J.; Chu, S.; Marcelli, A.; Chu, W.; Wu, D.; Qian, B.; Tao, S.; Song, L. Rational design of hierarchical FeSe₂ encapsulated with bifunctional carbon cuboids as an advanced anode for sodium-ion batteries. *Nanoscale* **2020**, *12*, 22210–22216. [[CrossRef](#)] [[PubMed](#)]
133. Pan, Q.; Zhang, M.; Zhang, L.; Li, Y.; Li, Y.; Tan, C.; Zheng, F.; Huang, Y.; Wang, H.; Li, Q. FeSe₂@C Microrods as a Superior Long-Life and High-Rate Anode for Sodium Ion Batteries. *ACS Nano* **2020**, *14*, 17683–17692. [[CrossRef](#)] [[PubMed](#)]
134. Shi, N.; Chu, Y.; Xi, B.; Huang, M.; Chen, W.; Duan, B.; Zhang, C.; Feng, J.; Xiong, S. Sandwich Structures Constructed by ZnSe@N-C@MoSe₂ Located in Graphene for Efficient Sodium Storage. *Adv. Energy Mater.* **2020**, *10*, 2002298. [[CrossRef](#)]
135. Wang, T.; Guo, W.; Wang, G.; Wang, H.; Bai, J.; Wang, B. Highly dispersed FeSe₂ nanoparticles in porous carbon nanofibers as advanced anodes for sodium and potassium ion batteries. *J. Alloys Compd.* **2020**, *834*, 155265. [[CrossRef](#)]
136. Xiong, Z.; Sun, D.; Jia, X.; Zhou, J. Core/shell FeSe/carbon nanosheet-assembled microflowers with ultrahigh coulombic-efficiency and rate performance as nonpresodiate anode for sodium-ion battery. *Carbon* **2020**, *166*, 339–349. [[CrossRef](#)]
137. Gao, X.; Kuai, Y.; Xu, Z.; Cao, Y.; Wang, N.; Hirano, S.I.; Nuli, Y.; Wang, J.; Yang, J. SnSe₂/FeSe₂ Nanocubes Capsulated in Nitrogen-Doped Carbon Realizing Stable Sodium-Ion Storage at Ultrahigh Rate. *Small Methods* **2021**, *5*, e2100437. [[CrossRef](#)] [[PubMed](#)]
138. Xiao, S.; Li, X.; Zhang, W.; Xiang, Y.; Li, T.; Niu, X.; Chen, J.S.; Yan, Q. Bilateral Interfaces in In₂Se₃-CoIn₂-CoSe₂ Heterostructures for High-Rate Reversible Sodium Storage. *ACS Nano* **2021**, *15*, 13307–13318. [[CrossRef](#)]

139. Xin, W.; Chen, N.; Wei, Z.; Wang, C.; Chen, G.; Du, F. Self-Assembled FeSe₂ Microspheres with High-Rate Capability and Long-Term Stability as Anode Material for Sodium- and Potassium-Ion Batteries. *Chemistry* **2021**, *27*, 3745–3752. [[CrossRef](#)]
140. Zhang, Y.; Wu, Y.; Zhong, W.; Xiao, F.; Kashif Aslam, M.; Zhang, X.; Xu, M. Highly Efficient Sodium-Ion Storage Enabled by an rGO-Wrapped FeSe₂ Composite. *ChemSusChem* **2021**, *14*, 1336–1343. [[CrossRef](#)]
141. Wang, Z.-Q.; Zeng, B.; Zhou, D.; Tai, L.; Liu, X.-D.; Lau, W.-M. Rich-oxygen-doped FeSe₂ nanosheets with high pseudocapacitance capacity as a highly stable anode for sodium ion battery. *Chem. Eng. J.* **2022**, *428*, 132637. [[CrossRef](#)]
142. Yi, Y.; Du, X.; Zhao, Z.; Liu, Y.; Guan, H.; Liu, X.; Pei, X.; Zhang, S.; Li, D. Coupling of Metallic VSe₂ and Conductive Polypyrrole for Boosted Sodium-Ion Storage by Reinforced Conductivity Within and Outside. *ACS Nano* **2022**, *16*, 7772–7782. [[CrossRef](#)] [[PubMed](#)]
143. Wu, L.; Gao, J.; Qin, Z.; Sun, Y.; Tian, R.; Zhang, Q.; Gao, Y. Deactivated-desulfurizer-derived hollow copper sulfide as anode materials for advanced sodium ion batteries. *J. Power Sources* **2020**, *479*, 228518. [[CrossRef](#)]
144. Je, J.; Lim, H.; Jung, H.W.; Kim, S.O. Ultrafast and Ultrastable Heteroarchitected Porous Nanocube Anode Composed of CuS/FeS₂ Embedded in Nitrogen-Doped Carbon for Use in Sodium-Ion Batteries. *Small* **2022**, *18*, e2105310. [[CrossRef](#)] [[PubMed](#)]
145. Liu, Z.; Li, H.; He, Y.; Sun, H.; Xu, C.; Li, H.; Wang, X.; Zhang, G.; Sun, Z.; Wei, Q.; et al. An integrated strategy based on Schiff base reactions to construct unique two-dimensional nanostructures for intrinsic pseudocapacitive sodium/lithium storage. *Chem. Eng. J.* **2022**, *429*, 132339. [[CrossRef](#)]
146. Peng, B.; Lv, Z.; Xu, S.; Pan, J.; Zhao, W.; Dong, C.; Huang, F. Tailoring Ultrafast and High-Capacity Sodium Storage via Binding-Energy-Driven Atomic Scissors. *Adv. Mater.* **2022**, *34*, e2200863. [[CrossRef](#)] [[PubMed](#)]
147. Sun, Z.; Wu, X.; Gu, Z.; Han, P.; Zhao, B.; Qu, D.; Gao, L.; Liu, Z.; Han, D.; Niu, L. Rationally designed nitrogen-doped yolk-shell Fe₇Se₈/Carbon nanoboxes with enhanced sodium storage in half/full cells. *Carbon* **2020**, *166*, 175–182. [[CrossRef](#)]
148. Huang, P.; Zhang, S.; Ying, H.; Zhang, Z.; Han, W. Few-layered Ti₃C₂ MXene anchoring bimetallic selenide NiCo₂Se₄ nanoparticles for superior Sodium-ion batteries. *Chem. Eng. J.* **2021**, *417*, 129161. [[CrossRef](#)]
149. Zhang, Y.; Huang, X.L.; Tan, P.; Bao, S.; Zhang, X.; Xu, M. Ultrafast kinetics and high capacity for Stable Sodium Storage enabled by Fe₃Se₄/ZnSe heterostructure engineering. *Composites Part B* **2021**, *224*, 109166. [[CrossRef](#)]
150. Huang, Z.; Zhou, S.; Dai, P.; Zeng, Y.; Huang, L.; Liao, H.G.; Sun, S.G. Insights into Electrochemical Processes of Hollow Octahedral Co₃Se₄@rGO for High-Rate Sodium Ion Storage. *ACS Appl. Mater. Interfaces* **2022**, *14*, 37689–37698. [[CrossRef](#)]
151. Wu, H.; Yuan, R.; Li, M.; Liu, L.; Liu, Y.; Song, Q.; Ai, W.; Du, H.; Du, Z.; Wang, K. Co_{0.85}Se–Fe₇Se₈ nanocuboids embedded in reduced graphene oxides as cycle-stable anodes for sodium-ion batteries. *Carbon* **2022**, *198*, 171–178. [[CrossRef](#)]
152. Yue, L.; Wang, D.; Wu, Z.; Zhao, W.; Ren, Y.; Zhang, L.; Zhong, B.; Li, N.; Tang, B.; Liu, Q.; et al. Polyrrole-encapsulated Cu₂Se nanosheets in situ grown on Cu mesh for high stability sodium-ion battery anode. *Chem. Eng. J.* **2022**, *433*, 134477. [[CrossRef](#)]
153. Zhao, W.; Ma, X.; Yue, L.; Zhang, L.; Luo, Y.; Ren, Y.; Zhao, X.-E.; Li, N.; Tang, B.; Liu, Q.; et al. A gradient hexagonal-prism Fe₃Se₄@SiO₂@C configuration as a highly reversible sodium conversion anode. *J. Mater. Chem. A* **2022**, *10*, 4087–4099. [[CrossRef](#)]
154. Wu, H.; Wang, K.; Li, M.; Wang, Y.; Zhu, Z.; Liang, J.; Du, Z.; Ai, W.; He, S.; Yuan, R.; et al. Double-Walled NiTeSe–NiSe₂ Nanotubes Anode for Stable and High-Rate Sodium-Ion Batteries. *Small* **2023**, *19*, 2300162. [[CrossRef](#)] [[PubMed](#)]
155. Gim, H.; Maulana, A.Y.; Choi, J.; Song, J.; Yun, B.; Jeong, Y.; An, N.; Park, M.; Futralan, C.M.; Kim, J. One dimensional pea-shaped NiSe₂ nanoparticles encapsulated in N-doped graphitic carbon fibers to boost redox reversibility in sodium-ion batteries. *J. Mater. Sci. Technol.* **2024**, *168*, 215–226. [[CrossRef](#)]
156. Xiong, Z.; Shi, H.; Zhang, W.; Yan, J.; Wu, J.; Wang, C.; Wang, D.; Wang, J.; Gu, Y.; Chen, F.-R.; et al. In Situ Growth of Iron Sulfide on Fast Charge Transfer V₂C-MXene for Superior Sodium Storage Anodes. *Small* **2023**, *19*, 2206767. [[CrossRef](#)]
157. Hu, M.; Zhang, H.; Yang, L.; Lv, R. Ultrahigh rate sodium-ion storage of SnS/SnS₂ heterostructures anchored on S-doped reduced graphene oxide by ion-assisted growth. *Carbon* **2019**, *143*, 21–29. [[CrossRef](#)]
158. Sun, S.; Zang, J.; Ruan, J.; Fang, F.; Sun, D.; Song, Y.; Wang, F. Two-Dimensional CuGaSe₂@ZnSe-NC Heterostructures for Enhanced Sodium Ion Storage. *ACS Appl. Energy Mater.* **2021**, *4*, 2761–2768. [[CrossRef](#)]
159. Sun, W.; Zhao, W.; Yuan, S.; Zhang, L.; Yang, Y.; Ge, P.; Ji, X. Designing Rational Interfacial Bonds for Hierarchical Mineral-Type Trogtalite with Double Carbon towards Ultra-Fast Sodium-Ions Storage Properties. *Adv. Funct. Mater.* **2021**, *31*, 2100156. [[CrossRef](#)]
160. Zheng, Y.; Wei, S.; Shang, J.; Wang, D.; Lei, C.; Zhao, Y. High-Performance Sodium-Ion Batteries Enabled by 3D Nanoflowers Comprised of Ternary Sn-Based Dichalcogenides Embedded in Nitrogen and Sulfur Dual-Doped Carbon. *Small* **2023**, *19*, e2303746. [[CrossRef](#)]
161. Zheng, H.; Wang, J.; Li, H.; Deng, S.; Zuo, Y.; Yan, W.; Zhang, J. Constructing a novel heterostructure of NiSe₂/CoSe₂ nanoparticles with boosted sodium storage properties for sodium-ion batteries. *J. Mater. Chem. A* **2022**, *10*, 16268–16279. [[CrossRef](#)]
162. Hu, X.; Qiu, M.; Liu, Y.; Yuan, J.; Chen, J.; Zhan, H.; Wen, Z. Interface and Structure Engineering of Tin-Based Chalcogenide Anodes for Durable and Fast-Charging Sodium Ion Batteries. *Adv. Energy Mater.* **2022**, *12*, 2202318. [[CrossRef](#)]
163. Liu, Y.; Yang, Z.; Wang, E.; Kuang, Q.; Ming, Y.; Zhong, B.; Wu, Z.; Guo, X. Optimization of Ni_xCo_{1-x-y}Mn_ySe₂ composition for efficient sodium storage. *Chem. Eng. J.* **2023**, *456*, 140951. [[CrossRef](#)]

Disclaimer/Publisher's Note: The statements, opinions and data contained in all publications are solely those of the individual author(s) and contributor(s) and not of MDPI and/or the editor(s). MDPI and/or the editor(s) disclaim responsibility for any injury to people or property resulting from any ideas, methods, instructions or products referred to in the content.